Porosity-dependent stability analysis of bio-inspired cellular nanocomposite shells

Aragh, B. Sobhani; Tan, W.; Farahani, E. Borzabadi; Al-Greer, M.; Hughes, D.

Published in:
International Journal of Mechanical Sciences

Link to article, DOI:
10.1016/j.ijmecsci.2023.108763

Publication date:
2024

Document Version
Publisher's PDF, also known as Version of record

International Journal of Mechanical Sciences 263 (2024) 108763

Contents lists available at ScienceDirect

International Journal of Mechanical Sciences

journal homepage: www.elsevier.com/locate/ijmecsci

Porosity-dependent stability analysis of bio-inspired cellular nanocomposite shells

B. Sobhani Aragh [a,*], W. Tan [b], E. Borzabadi Farahani [c], M. Al-Greer [a], D. Hughes [a]

[a] School of Computing, Engineering and Digital Technologies, Teesside University, Tees Valley, Middlesbrough, TS1 3BX, United Kingdom
[b] School of Engineering and Materials Science, Queen Mary University of London, London E1 4NS, United Kingdom
[c] Department of Wind Energy, Technical University of Denmark, Frederiksborgvej 399, 4000 Roskilde, Denmark

ARTICLE INFO

Keywords:
Closed-cell cellular
Carbon nanotubes
Effective material properties
Buckling analysis
Porous nanocomposites

ABSTRACT

This paper presents an innovative numerical model to investigate buckling behaviour of bio-inspired continuously graded porous (CGP) nanocomposite cylindrical shells. It is postulated that the shell subjected to combined lateral pressure and axial compressive load is constructed from metal foams with closed-cell structures that possess graded internal pores, which exhibit three types of continuously graded porosity profiles based on a power-law distribution. A scaling relation for the effective Young's modulus of the cellular structure determined by a variational finite element method (FEM) is used. The effective constitutive law of an elastic isotropic metal matrix containing distributed elastic carbon-nanotubes (CNTs) is estimated in consideration of the impact of CNTs agglomeration using a continuum model based on the Eshelby–Mori–Tanaka (EMT) approach. In contrast to conventional approaches, the study employs Euler–Bernoulli beams to model stiffeners within the CGP shells. This choice allows for a more realistic representation of stiffener effects, as opposed to the prevalent approach of uniform smearing across the shell's surface. The equilibrium equations of the CGP shell, based on the Reddy higher-order shell theory (RHST), is obtained through the application of the Euler equation. Subsequently, the equations for stability are obtained through the utilization of the variational method. This study emphasizes the effects of geometrical parameters, porosity variability, and distribution of CNTs on the buckling performance of the CGP shells. The intricate interplay between CNTs and porosity distributions critically influences the stability behaviour of CGP shells. CNTs arrangement remarkably impacts buckling behaviour at higher length-to-mean radius ratios, while symmetric porosity near the mid-surface significantly enhances stiffness. These findings provide valuable insights for designing closed-cell cellular stiffened shells with optimal porosity to enhance stability.

1. Introduction

Recently, concerns over the prospect of climate change and limited resources of materials and energy have stimulated a pressing demand for the development of resilient and efficient lightweight structures with outstanding multi-functional properties. Moreover, recent advances in high-tech industries require innovative engineering designs to address the tunable multi-functional mechanical properties, including high strength, stiffness, toughness, and energy absorption. Porous cellular materials are one of the emerging lightweight materials that can simultaneously fulfil multiple requirements from structural stiffness to thermal insulation. For instance, a captivating potential of sandwich porous metal foams shines in their role in creating the front structure of high-speed trains, shown in Fig. 1. This application merges lightweight design with structural integrity for pioneering the future of swift and efficient rail travel. Metal foams are porous materials that find extensive application in automotive industry [1], energy storage systems [2–4], civil constructions [5], biomedical engineering [6], and aerospace engineering [7]. These materials can be classified into two types, namely open-cell and closed-cell metal foams. The internal pores of the latter exhibit interconnectivity while the former displays significant separation via thin cell walls. This structural variation yields significant differences in performance, leading to the optimal function of one metal foam over the other depending on the specific application.

The vast majority of the available works on the metal foams have been riveted on the uniform or random distribution of porosities. Recent attention has been given to achieving economic multi-functionality in metal foams through tailored control of internal pore size and density, in one or more directions, inspired by the concept of bio-inspired functionally graded materials (FGMs) [8–10]. Biological materials utilize diverse strategies to mitigate stress concentrations at interfaces,

* Corresponding author.
E-mail address: b.sobhaniaragh@tees.ac.uk (B. Sobhani Aragh).

https://doi.org/10.1016/j.ijmecsci.2023.108763
Received 8 July 2023; Received in revised form 27 August 2023; Accepted 15 September 2023
Available online 23 September 2023

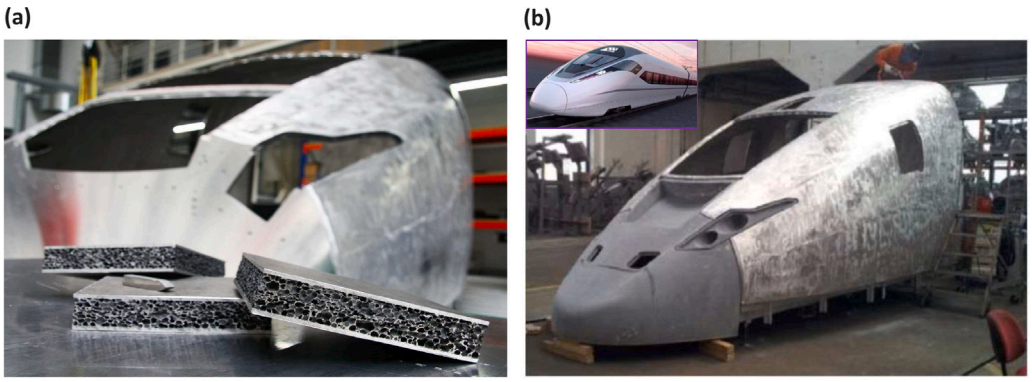

Fig. 1. (a) Prototype a 25-millimeter-thick layer made of porous foam. **(b)** Highly porous aluminum alloy foam used in the fabrication of the frontal structure of the Intercity-Express-Train (ICE) train, jointly developed by Voith Engineering and the Fraunhofer Institute for Machine Tools and Forming Technology (IWU). [21,22].

including the implementation of gradual transitions in either chemical compositions or microstructural characteristics [11]. This phenomenon is exemplified in the squid beaks [12], which exhibit a gradual shift from stiff to compliant materials, as well as in the variation of porosity observed between trabecular and cortical bones [13]. This has led to the emergence of the novel continuously graded porous (CGP) structures comprised of metal foams. Various theoretical models have been introduced to predict the vibrational and buckling behaviour of CGP beams and plates [14–20]. However, despite the significant importance of cylindrical shells in various engineering disciplines such as mechanical, civil, ocean, and aeronautical engineering, there has been a scarcity of research dedicated to studying the stability of CGP shells.

In recent years, there has been a growing interest in investigating the stability and buckling behaviour of bio-inspired FG shells and plates, driven by their potential applications in diverse engineering fields [23–28]. Duc et al. [29] conducted an investigation into the nonlinear buckling and post-buckling analyses of stiffened truncated conical sandwich shells. These shells were composed of functionally graded (FG) face sheets and a CGP core, and rested on the Winkler–Pasternak elastic foundation. The stability equations for the shell were derived using the first-order shear deformation theory (FSDT), incorporating a von Karman–Donnell type of kinematic non-linearity. Zhou et al. [30] conducted a nonlinear buckling analysis on cylindrical shells composed of FG porous graphene platelet-reinforced composites, considering pre-buckling effects and in-plane constraints. Their findings indicate that the optimal material distribution for this type of nanocomposite is a symmetrical distribution of both graphene platelets and porosity throughout the thickness of the shell. Nam et al. [31] conducted a study on the nonlinear buckling and post-buckling of cylindrical shells reinforced by orthogonal stiffeners resting on Pasternak elastic foundations, utilizing classical shell theory as the basis for their investigation. An investigation into the dynamic buckling analysis of a truncated conical shell made of FGMs was conducted by Allahkarami et al. [32]. The shell was embedded in an elastic foundation and subjected to an excitation compressive load. The study utilized FSDT to model the behaviour of the shell under these conditions. Twinkle and Pitchaimani [33] presented the buckling and vibration characteristics of cylindrical shells reinforced with CGP graphene platelets. The effective mechanical properties of open-cell metal foams were evaluated using a modified Halpin–Tsai micro-mechanics model, in combination with an extended rule of mixture. A finite element model was developed by Zghal and Dammak [34] to demonstrate the impact of porosity parameter on the critical buckling responses of power-based (P-FGM) and sigmoid (S-FGM) plates and spherical caps in FGMs. This model was developed in the context of FSDT. The researchers utilized this approach to investigate the relationship between porosity parameter and buckling behaviour. Thai et al. [35] presented an analytical method for examining the nonlinear instability of eccentrically stiffened FG sandwich truncated conical shells with porosity in the presence of Pasternak elastic foundations. The approach employed is based on displacement approach. A buckling analysis on a cylindrical shell made of porous nanocomposite reinforced with graphene platelet was conducted by Shahgholian et al. [36] based on the FSDT. The researchers computed various mechanical properties, including the effective modulus of elasticity in the thickness direction, by applying the modified Halpin–Tsai micro-mechanics approach. Additionally, they utilized the rule of mixture to determine density and Poisson's ratio. Tao and Dai [37] carried out a geometrically nonlinear analysis on sandwich FG cylindrical shells with a porous core to investigate their post-buckling behaviour when subjected to central point loads and uniform pressures. They used higher-order shear deformation theories (HSDT) and a non-uniform rational B-spline (NURBS)-based isogeometric analysis (IGA) in combination with the modified arc-length method of Crisfield. The study aimed to obtain load–deflection responses and identify snap-through and snap-back post-buckling behaviours.

The constraints of the classical theories [38] and the FSDT [39–41] stimulated scholars to develop a number of HSDT [42–44]. Among several kinds of the HSDT, the Reddy higher order shell theory (RHST) [45,46] with five unknowns is the most broadly employed theory in the research of plate and shell structures due to adequate efficiency and straightforwardness without any shear correction coefficient. A concise review on the plate and shell laminate theories have been recently presented by Sobhani Aragh et al. [47]. What is more, the shells are commonly strengthened by stiffening components for the purpose of improving load-carrying capacity with a relatively little additional weight. Rings and stringers, which are circumferential and meridional stiffeners, respectively, have widespread usage in a myriad of engineering application [48]. When lightweight shells with porosities are subjected to a mechanical loading, they might be buckled despite comparatively increased critical buckling loading as a result of utilizing stiffeners. Therefore, there is a necessity to investigate the buckling behaviour of such structures for multi-purpose and cost-effective design with improved performance.

Studies have shown that the mechanical properties of nanocomposites can be enhanced by integrating carbon-nanotubes (CNTs) into metallic matrices. In the last years, the commonly-used techniques for the fabrication of CNT–metal matrix composites have included spark plasma sintering [49,50], hot isostatic pressing [51], microwave sintering [50], and electrochemical deposition [52]. Selective laser melting (SLM) [53] and laser powder bed fusion (LPBF) [54] methods of additive manufacturing (AM) have garnered significant attention due to their ability to produce metallic parts with intricate geometries [55,56]. Advanced techniques enable the production of components directly from 3-D CAD models through the selective melting and solidification of thin layers of loose powder using high-energy laser beams in a layer-by-layer manner. Gu et al. [57] utilized a laser-assisted am technique known as SLM to produce nanocomposites composed of Al

and CNTs that possess customized microstructures and impressive mechanical properties. Meanwhile, Yu et al. [58] achieved the successful production of AlSi10Mg nanocomposites reinforced with multi-walled carbon nanotubes (MWCNTs) at a mass fraction of 0.5% through the utilization of SLM. In a recent work by Yin et al. [59], CNT/316L stainless steel nanocomposites were fabricated by mixing 316L stainless steel powders with various content ratios of CNT through ball milling followed by LPBF. Analysis of the scanning electron microscopy (SEM) images [60,61] revealed that the resulting nanocomposites exhibited CNT aggregation, which resulted in localized areas of higher CNT concentration than the average volume fraction throughout the material. In recent years, a substantial body of literature has been focused on investigating the effects of nanomaterials, specifically CNTs, on the structural behaviour of engineered systems [62–71]. Sobhani Aragh et al. [72–74] conducted a study where they used the Eshelby–Mori–Tanaka (EMT) approach, an effective homogenization technique, to examine how the degree of CNT aggregation within the ceramic matrix phase affects the mechanical response of nanocomposite shells. The interested readers are encouraged to refer to Sobhani Aragh's PhD thesis [75] to find comprehensive details on various homogenization techniques.

Motivated by the lack of research work on mechanical buckling of CGP stiffened cylindrical shells strengthened by agglomerated CNTs, this paper aims to bridge this gap by presenting an effective numerical model to investigate buckling behaviour CGP nanocomposite shells. The main contribution of this work is shed light on the effects of porosities as well as CNTs distributions through the shell's thickness on the stability of the shell. Depending on how eccentrically the stiffeners are positioned in relation to the mid-surface of the shell, two types of stiffeners, i.e. internal and exterior, are considered. The smeared stiffener method is employed under the premise of a tightly spaced configuration of stiffeners. The EMT technique is utilized to develop a continuum model for estimating the effective constitutive law of an elastic isotropic metal matrix containing scattered elastic inhomogeneities in the form of CNTs. The shell under combined lateral pressure and axial compressive load is assumed to be composed of closed-cell metal foams that possess graded internal pores, which exhibit Classic, Symmetric, and Asymmetric distributions of porosity based on a power-law distribution. A scaling correlation for the Young's modulus of closed-cell cellular solids is employed, which is obtained through the application of a variational finite element method (FEM).

2. Methodology

The geometrical configuration of a CGP open cylindrical shell with mean radius R, thickness h and length L, is shown in Fig. 2. The three orthogonal displacements of an arbitrary point on the shell middle surface in α_1, α_2, and α_3 directions are represented as u_1, u_2 and u_3, respectively. The CGP nanocomposite shell is reinforced by eccentrically closely spaced circular rings and longitudinal stringers with the width and thickness of circular and longitudinal stiffeners d_r, h_r and d_s, h_s, respectively. It is worth highlighting that the investigated shell is subjected to a concurrent application of lateral pressure and axial compressive load. In the present work, the shell is made of closed-cell porous nanocomposite where the porosity coefficient and total volume fraction of the CNTs are constant throughout the shell, however, they smoothly vary along the thickness direction.

2.1. Micro-mechanical modelling of accumulated CNTs

As reported in several SEM images [61], CNTs highly tend to agglomerate in the matrix phase, which can be attributed to their low bending stiffness and high aspect ratio. In this part, the effective mechanical characteristics of the nanocomposite shells are determined using a two-parameter EMT model [72,73]. The primary limitation of the original elastic inclusion theory proposed by Eshelby is that it assumes the consideration of a solitary inclusion within a semi-infinite elastic medium that is isotropic and homogeneous. This can be alleviated by developing the Mori–Tanaka approach to consider the presence of several inhomogeneities within in a finite region [77]. In other words, the EMT method is primarily based on combining Eshelby's concept of equivalent elastic inclusions [78] with Mori–Tanaka's idea of average stress across the matrix phase [79]. Inclusions possessing distinct material properties from the surrounding regions are identified in areas exhibiting a high concentration of CNTs. The arrangement of CNTs within a metal matrix phase is determined by their location relative to the inclusions, either inside or outside. The overall volume fraction of the reinforcing phase consisting of CNTs is divided into two components

$$V_c = V_c^{inc} + V_c^{m} \tag{1}$$

where V_c^{inc} and V_c^{m} denote the volume fraction of CNTs situated in the inclusions and distributed through the metal matrix phase, respectively. The presence of agglomerated CNTs in a metal matrix results in the deterioration of elastic properties within the resulting nanocomposite. This phenomenon can be qualitatively explained by proposing two accumulation parameters, denoted as δ and γ, given by

$$\delta = \frac{V^{inc}}{V}\ , \tag{2}$$

$$\gamma = \frac{V_c^{inc}}{V_c} \tag{3}$$

where V^{inc} denotes the effective volume fraction of the inclusions, and the parameter δ is the volume fraction of inclusions in relation to the overall volume fraction V of the representation volume element (RVE). Provided that parameter δ is equal to unity, the CNTs are not accumulating in the metal matrix phase. In other words, there is only one spherical inclusion, which practically coincides with the total volume fraction. Moreover, an increase of the parameter δ leads to the decline of the accumulation degree of CNTs. Moreover, the parameter γ specifies the ratio of CNTs volume fraction situated in the inclusions to the total volume fraction of the CNTs. It is apparent that, when γ is equal to one, all CNTs are contained within the inclusions. It is noteworthy to mention that a specific constraint must be satisfied in order for the accumulation of CNTs to occur as

$$\gamma > \delta \tag{4}$$

Mori and Tanaka [79] have developed an approach to evaluate the effective stiffness tensor. The basic idea is to consider the interaction between the inhomogeneities through their effect on the mean values of the fields in the matrix phase. Benveniste's revisitation [80] provides the expression for the effective elastic tensor, which is as follows [81]

$$\mathbb{C} = \mathbb{C}_m + f_c < \left(\mathbb{C}_m - \mathbb{C}_m\right) : \mathbb{A}^{MT} > : \left[f_m \mathbb{I} + f_c < \mathbb{A}^{MT} >\right]^{-1} \tag{5}$$

where

$$\mathbb{A}^{MT} = \left[\mathbb{I} + \mathbb{S} : \mathbb{C}_m^{-1} : \left(\mathbb{C}_c - \mathbb{C}_m\right)\right]^{-1} \tag{6}$$

where $\mathbb{I}$ denotes the fourth-order unit tensor, $\mathbb{S}$ represents the fourth-order Eshelby tensor [78], which is specialized to the inhomogeneities with cylindrical geometry, representative of the straight and long CNTs, $\mathbb{A}^{MT}$ is a fourth-order tensor referred to as concentration factor, and the brackets denote an average. The subscripts m and c stand for the quantities of the matrix and the CNT reinforcing phase, respectively, f_m and f_r denote the volume fractions of the respective phases.

The effective bulk modulus $K_{in}(\alpha_3)$ and shear modulus $G_{in}(\alpha_3)$ of spherical inclusions containing randomly arranged transversely isotropic CNTs are calculated using the EMT method as

$$K_{in}(\alpha_3) = K_m + \frac{f_c(\alpha_3)\gamma(\delta_c - 3K_m\alpha_c)}{3(\delta - f_c(\alpha_3)\gamma + f_c(\alpha_3)\gamma\alpha_c)} \tag{7}$$

$$G_{in}(\alpha_3) = G_m + \frac{f_c(\alpha_3)\gamma(\eta_c - 2G_m\beta_c)}{2(\delta - f_c(\alpha_3)\gamma + f_c(\alpha_3)\gamma\alpha_c)} \tag{8}$$

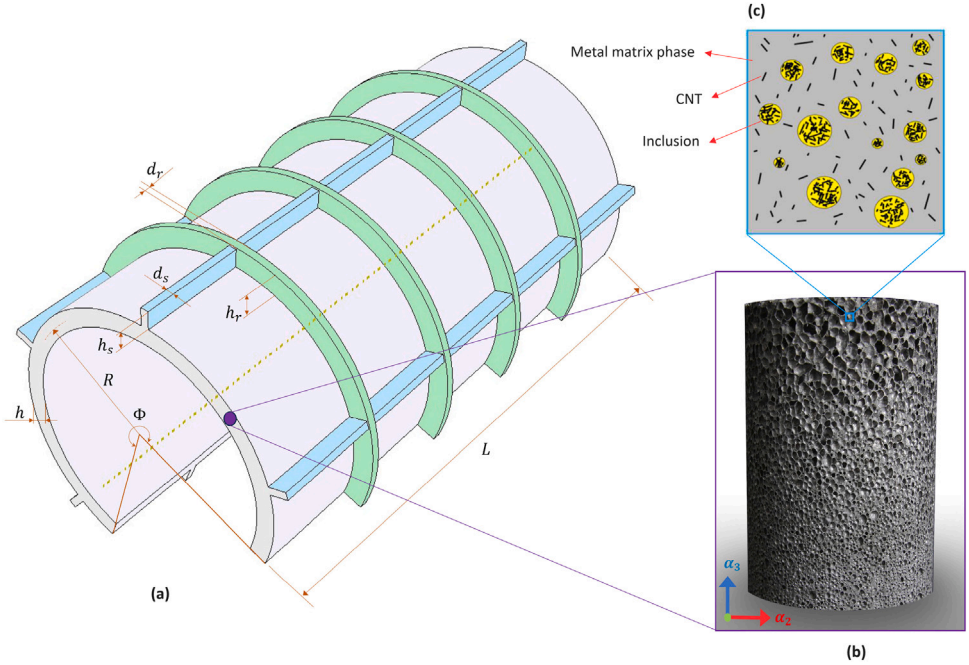

Fig. 2. **(a)** Schematic configuration of a CGP shell strengthened by rings and stringers. **(b)** Cross-sectional image of the shell showing the varying pore size along the thickness direction [76]. **(c)** Visual representation illustrating the arrangement of CNTs within inclusions and their dispersion throughout the metal matrix phase at the meso-scale.

Similarly, the effective bulk modulus $K_{out}(\alpha_3)$ and shear modulus $G_{out}(\alpha_3)$ of the metal matrix phase are elaborated as

$$K_{out}(\alpha_3) = K_m + \frac{f_c(\alpha_3)(1-\gamma)(\delta_c - 3K_m\alpha_c)}{3(1-\delta-f_c(\alpha_3)(1-\gamma)+f_c(\alpha_3)(1-\gamma)\alpha_c)} \tag{9}$$

$$G_{out}(\alpha_3) = G_m + \frac{f_c(\alpha_3)(1-\gamma)(\eta_c - 2G_m\beta_c)}{2(1-\delta-f_c(\alpha_3)(1-\gamma)+f_c(\alpha_3)(1-\gamma)\beta_c)} \tag{10}$$

where K_m and G_m represent the bulk and shear moduli of the metal matrix, respectively, and α_c, β_c, δ_c, and η_c are defined by

$$\alpha_c = \frac{3(K_m+G_m)+k_c+l_c}{3(G_m+k_c)} \tag{11}$$

$$\beta_c = \frac{1}{5}\left[\frac{4G_m+2k_c+l_c}{3(G_m+k_c)} + \frac{4G_m}{G_m+p_c} + \frac{2\left[G_m(3K_m+G_m)+G_m(3K_m+7G_m)\right]}{G_m(3K_m+G_m)+m_c(3K_m+7G_m)}\right] \tag{12}$$

$$\delta_c = \frac{1}{3}\left[n_c + 2l_c + \frac{(2k_c+l_c)(3K_m+2G_m-l_c)}{G_m+k_c}\right] \tag{13}$$

$$\eta_c = \frac{1}{5}\left[\frac{2}{3}(n_c-l_c) + \frac{8G_mp_c}{G_m+p_c} + \frac{2(k_c-l_c)(2G_m+l_c)}{3(G_m+k_c)} + \frac{8m_cG_m(3K_m+4G_m)}{3K_m(m_c+G_m)+G_m(7m_c+G_m)}\right] \tag{14}$$

where k_c, m_c, n_c and l_c denote the Hill's elastic moduli for the reinforcing phase. Ultimately, the effective bulk modulus and shear modulus of the nanocomposite are obtained by

$$K(\alpha_3) = K_{out}(\alpha_3)\left[1 + \frac{\delta\left(\frac{K_m}{K_{out}(\alpha_3)}-1\right)}{1+\kappa_1(z)(1-\delta)\left(\frac{K_m}{K_{out}(\alpha_3)}-1\right)}\right] \tag{15}$$

$$G(\alpha_3) = G_{out}(\alpha_3)\left[1 + \frac{\delta\left(\frac{G_m}{G_{out}(\alpha_3)}-1\right)}{1+\kappa_2(\alpha_3)(1-\delta)\left(\frac{G_m}{G_{out}(\alpha_3)}-1\right)}\right] \tag{16}$$

where

$$\kappa_1(\alpha_3) = \frac{1+\upsilon_{out}(\alpha_3)}{3(1-\upsilon_{out}(\alpha_3))} \tag{17}$$

$$\kappa_2(\alpha_3) = \frac{2(4-5\upsilon_{out}(\alpha_3))}{3(1-\upsilon_{out}(\alpha_3))} \tag{18}$$

in which $\upsilon_{out}(\alpha_3)$ represents the Poisson's ratio of the metal matrix phase as

$$\upsilon_{out}(\alpha_3) = \frac{3K_{out}(\alpha_3)-2G_{out}(\alpha_3)}{2\left[3K_{out}(\alpha_3)+G_{out}(\alpha_3)\right]} \tag{19}$$

In above-mentioned formulations, $f_c(\alpha_3)$ and $f_m(\alpha_3)$ are the volume fraction of the CNTs and the metal phase, respectively, which fulfil the expression of $f_c(\alpha_3)+f_m(\alpha_3)=1$. The CNTs volume fraction is defined by a gradual change from the inner to the outer surface of the shell, proposing that

$$f_c(\alpha_3) = V_c^* V_c(\alpha_3) \tag{20}$$

where

$$V_c^* = \left[\frac{\rho_c}{w_c\rho_m} - \frac{\rho_c}{\rho_m} + 1\right]^{-1} \tag{21}$$

in which w_c denotes the mass fraction of CNTs, ρ_c and ρ_m are density of CNTs and matrix phase, respectively. $V_c(\alpha_3)$ is the distribution of CNTs along the thickness direction of the shell. This study considers the various distributions of CNTs through the shell's thickness, as classified by Jalali et al. [82]. The profiles examined are Pyramid, Inverted Pyramid, Sandglass, and Uniform.

2.2. Modelling of porosity dispersion

To improve the strength-to-weight ratio and energy absorbing capability of the structure, porous materials, such as metal foams, has provided unique potential for a number of engineering applications. In these state-of-the-art materials, embedding pores can significantly decrease the structural weight whereas a loss of structural stiffness is partially compensated by including a certain amount of CNTs. Currently, a new paradigm shift is taking place in designing of porous composite materials from uniform dispersion to continuously graded distribution of porosity. Consequently, tailoring the desired properties of the CGP shell is achievable by employing an appropriate pattern for the distribution of porosity through the shell's thickness, in addition

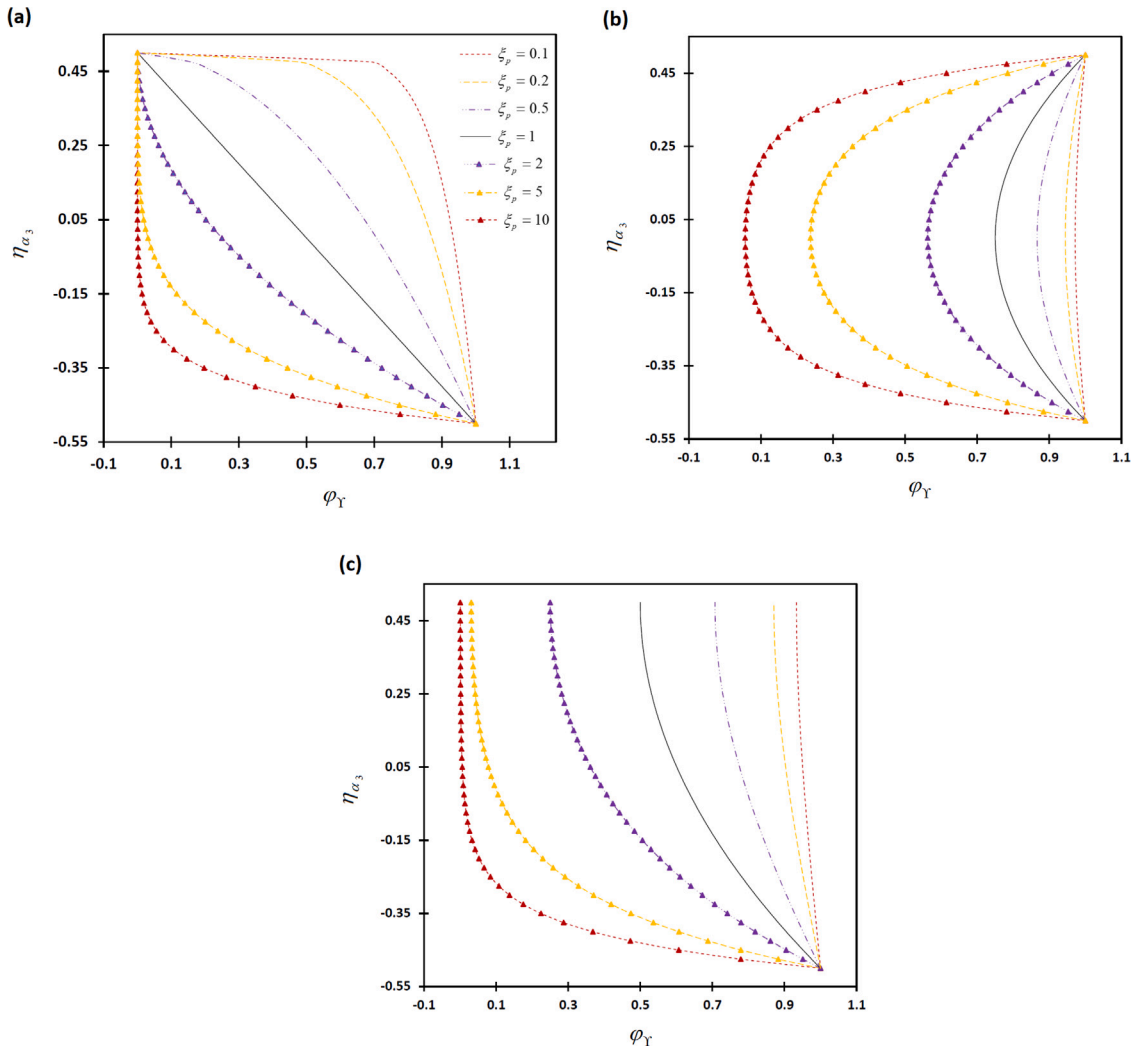

Fig. 3. Through-the-thickness variation of the function φ_Y in Eq. (23) for three key material profiles and different values of the parameter ξ_p ($\zeta = 2$). The function φ_Y governs the graded porosity distribution in the radial direction of the shell using a power-law distribution. **(a)** Classical profile ($a = 1,\ b = 0$). **(b)** Symmetric profile ($a = 1,\ b = 1$). **(c)** Asymmetric profile ($a = 1,\ b = 0.5$).

to Eq. (20) for the smooth variation of CNTs. This study concentrates on the closed-cell porous materials whose theoretical formulation for deriving the mechanical properties are different from those of open-cell materials. Nevertheless, this point has not been carefully notified in some literature [83–85]. The elastic moduli and density of the shell are estimated as

$$Y(\alpha_3) = Y_0\,\varphi_Y \tag{22}$$

where

$$\varphi_Y = \left[1 - a\left(\frac{1}{2} + \frac{\alpha_3}{h}\right) + b\left(\frac{1}{2} + \frac{\alpha_3}{h}\right)^{\zeta}\right]^{\xi_p} \tag{23}$$

$$\rho(\alpha_3) = \rho_0\,\varphi_\rho \tag{24}$$

where

$$\varphi_\rho = \left[1 - a\left(\frac{1}{2} + \frac{\alpha_3}{h}\right) + b\left(\frac{1}{2} + \frac{\alpha_3}{h}\right)^{\zeta}\right]^{\xi_m} \tag{25}$$

in which Y denotes either the effective Young's modulus or shear modulus of the nanocomposite shell and ρ represents the effective mass density. Subscripts 0 refers to the material properties of a perfect nanocomposite without any voids. ξ_p and ξ_m known as porosity coefficient and mass density coefficient, respectively. The function φ_Y governs through-the-thickness variation of Young's modulus, which have values that range from 0 to 1. In other words, it dominates the graded porosity distribution in the radial direction of the shell using a power-law distribution. For example, three key material profiles through the radial ($\eta_{\alpha_3} = (\alpha_3 - R)/h$) direction are illustrated in Figs. 3a–3c. The classical profile through the radial direction is presented as a case of the power-law distributions by setting $a = 1$ and $b = 0$. In Fig. 3a, the function φ_Y increases through the thickness from 0 at $\eta_{\alpha_3} = -0.5$ to 1 at $\eta_{\alpha_3} = 0.5$ for different values of the parameter ξ_p. By appropriate choice of the parameter ξ_p the porosity distribution can be regulated such that at η_{α_3} close to $\eta_{\alpha_3} = -0.5$, by rising the parameter ξ_p the rate of increase in Young's modulus grows while this trend is reversed at η_{α_3} close to $\eta_{\alpha_3} = 0.5$. By adjusting the values of a, b, and ζ, it is feasible to generate both symmetric and asymmetric profiles, as illustrated in Figs. 3b and 3c. Symmetric porosity distribution is achieved by setting $a = 1$, $b = 1$, and $\zeta = 2$ in Eq. (23). As can be seen in Fig. 3b, the function φ_Y on the inner surface is the same as that on the outer surface ($\varphi_Y = 1$), however, the Young's modulus drops with an increase in the parameter ξ_p and tends to $\varphi_Y = 0$ for higher values of parameter ξ_p. Fig. 3c demonstrates asymmetric profiles obtained by setting $a = 1$, $b = 0.5$, and $\zeta = 2$. This figure shows a specific case of the power-law distribution obtained by modifying the parameters

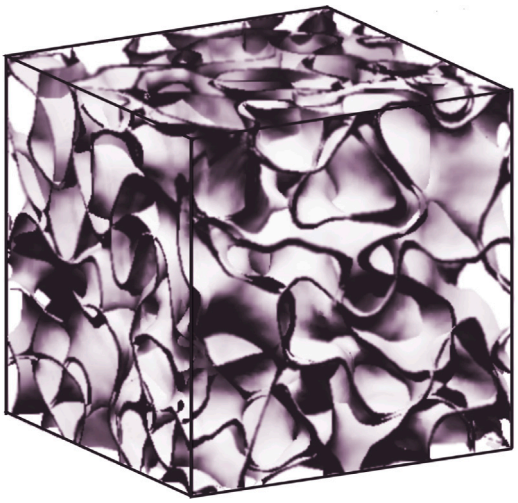

Fig. 4. 3-D Gaussian random field closed-cell model. [86].

a, b, and ζ. This profile is characterized by the fact that on the inner surface of shell we have a fixed value of $\varphi_Y = 1$ while on the outer surface the value of the function φ_Y is restrained by the parameter ξ_p. Moreover, the rate of growth in Young's modulus grows by increasing the parameter ξ_p at η_{α_3} near the inner surface.

A statistical closed-cell model based on Gaussian random fields (GRFs), which generates a substantial variation in cell sizes and shapes, has been established, as shown in Fig. 4 [86]. To predict the Young's modulus, a variational FEM was used. Based on the results obtained, a scaling relation can describe the Young's modulus of the model as

$$E(\alpha_3) = E_0\left(\frac{\rho(\alpha_3)/\rho_0 + 0.121}{1.121}\right)^{2.3}, \qquad 0.15 < \rho(\alpha_3)/\rho_0 < 1 \tag{26}$$

which is employed to obtain mass density coefficient, ξ_m, as

$$\xi_m = \frac{1.121\left(1 - \sqrt[2.3]{1 - \xi_p Y(\alpha_3)}\right)}{Y(\alpha_3)} \tag{27}$$

Note that $\xi_p = 0$ corresponds to a case when no pore exists in the nanocomposite while $\xi_p = 1$ is physically meaningless. With an increase in ξ_p, density and size of the pores in the material rise and, as a result, modulus of elasticity and mass density of the nanocomposite reduce. Furthermore, Poisson's ratio of the CGP shell is expressed as

$$\upsilon = 0.221\beta_0 + \upsilon_0\left(0.342{\beta_0}^2 - 1.21\beta_0 + 1\right) \tag{28}$$

where $\beta_0 = 1 - \rho(\alpha_3)/\rho_0$.

2.3. Fundamental formulations

Under the framework of the RHST, the displacements of a generic point at distance α_3 from the middle surface of the shell elaborated by (u_1, u_2, u_3) are related to the middle surface displacement by

$$\begin{aligned}
U_1(\alpha_1,\alpha_2,\alpha_3) &= u_1(\alpha_1,\alpha_2) + \alpha_3\left(\phi_1(\alpha_1,\alpha_2) + \frac{4}{3h^2}{\alpha_3}^2(\phi_1 + \partial u_3/\partial\alpha_1)\right)\\
U_2(\alpha_1,\alpha_2,\alpha_3) &= u_2(\alpha_1,\alpha_2) + \alpha_3\left(\phi_2(\alpha_1,\alpha_2) + \frac{4}{3h^2}{\alpha_3}^2(\phi_2 + \partial u_3/R\partial\alpha_2)\right)\\
U_3(\alpha_1,\alpha_2,\alpha_3) &= u_3(\alpha_1,\alpha_2)
\end{aligned} \tag{29}$$

where ϕ_1 and ϕ_2 are rotations at mid-surface of the shell with respect to α_1 and α_2. The nonlinear kinematic relations of the shell are defined by

$$\begin{Bmatrix}\varepsilon_{11}\\ \varepsilon_{22}\\ \gamma_{12}\end{Bmatrix} = \begin{Bmatrix}\varepsilon_{11}^{(0)}\\ \varepsilon_{22}^{(0)}\\ \gamma_{12}^{(0)}\end{Bmatrix} + \alpha_3\begin{Bmatrix}\varepsilon_{11}^{(1)}\\ \varepsilon_{22}^{(1)}\\ \gamma_{12}^{(1)}\end{Bmatrix} + {\alpha_3}^3\begin{Bmatrix}\varepsilon_{11}^{(3)}\\ \varepsilon_{22}^{(3)}\\ \gamma_{12}^{(3)}\end{Bmatrix} \tag{30}$$

$$\begin{Bmatrix}\gamma_{13}\\ \gamma_{23}\end{Bmatrix} = \begin{Bmatrix}\gamma_{13}^{(0)}\\ \gamma_{23}^{(0)}\end{Bmatrix} + {\alpha_3}^2\begin{Bmatrix}\gamma_{13}^{(2)}\\ \gamma_{23}^{(2)}\end{Bmatrix} \tag{31}$$

where

$$\begin{Bmatrix}\varepsilon_{11}^{(0)}\\ \varepsilon_{22}^{(0)}\\ \gamma_{12}^{(0)}\end{Bmatrix} = \begin{Bmatrix}u_{1,\alpha_1} + {w_{0,\alpha_1}^2}2\\ \upsilon_{2,\alpha_2} + \alpha_3 R + {u_{3,\alpha_2}^2}2\\ u_{1,\alpha_2} + u_{2,\alpha_1} + u_{3,\alpha_1}u_{3,\alpha_2}\end{Bmatrix}$$

$$,\begin{Bmatrix}\varepsilon_{11}^{(1)}\\ \varepsilon_{22}^{(1)}\\ \gamma_{12}^{(1)}\end{Bmatrix} = \begin{Bmatrix}\phi_{1,\alpha_1}\\ \phi_{2,\alpha_2}\\ \phi_{1,\alpha_2} + \phi_{2,\alpha_1}\end{Bmatrix}$$

$$\begin{Bmatrix}\varepsilon_{11}^{(3)}\\ \varepsilon_{22}^{(3)}\\ \gamma_{12}^{(3)}\end{Bmatrix} = -C_1\begin{Bmatrix}\phi_{1,\alpha_1} + u_{3,\alpha_1\alpha_1}\\ \phi_{2,\alpha_2} + u_{3,\alpha_2\alpha_2}\\ \phi_{1,\alpha_2} + \phi_{2,\alpha_1} + 2u_{3,\alpha_1\alpha_2}\end{Bmatrix} \tag{32}$$

$$\begin{Bmatrix}\gamma_{13}^{(0)}\\ \gamma_{23}^{(0)}\end{Bmatrix} = \begin{Bmatrix}\phi_1 + u_{3,\alpha_1}\\ \phi_2 + u_{3,\alpha_2}\end{Bmatrix}$$

$$\begin{Bmatrix}\gamma_{13}^{(1)}\\ \gamma_{23}^{(1)}\end{Bmatrix} = -3C_1\begin{Bmatrix}\phi_1 + u_{3,\alpha_1}\\ \phi_2 + u_{3,\alpha_2}\end{Bmatrix}$$

where ε_{11} and ε_{22} indicate the membrane strains, γ_{12}, γ_{23}, and γ_{13} represent the transverse shear strains. In Eq. (32), a comma denotes the partial differential operator. The constitutive equation of the shell is given by

$$\begin{aligned}
\sigma_{11} &= K_{11}\varepsilon_{11} + K_{12}\varepsilon_{22}\\
\sigma_{22} &= K_{21}\varepsilon_{11} + K_{22}\varepsilon_{22}\\
\tau_{23} &= K_{44}\gamma_{23}\\
\tau_{13} &= K_{55}\gamma_{13}\\
\tau_{12} &= K_{66}\gamma_{12}
\end{aligned} \tag{33}$$

in which K_{ij} are the elastic coefficients.

In most literature, the stiffener impact has been smeared over the stiffener spacing, which implies that the impact of discrete ring and stringers have not been accounted. Motivated by this, this paper considers ring and stringers as Euler–Bernoulli beams. Moreover, taking the Kirchhoff–Love assumptions into account, it is assumed that the straightness of the normal to the ring and stringers is preserved even after deformation. Consequently, the displacement fields of the stringer and ring are given, respectively, by

$$\begin{aligned}
\bar{u}_1(\alpha_1\,,\,\alpha_2) &= u_1^i(\alpha_1\,,\,\alpha_2) - \alpha_3\, u_{3,\alpha_1}^i(\alpha_1\,,\,\alpha_2)\\
\bar{u}_3(\alpha_1\,,\,\alpha_2) &= u_3^i(\alpha_1\,,\,\alpha_2)
\end{aligned} \tag{34}$$

$$\begin{aligned}
\bar{u}_1(\alpha_1\,,\,\alpha_2) &= u_2^i(\alpha_1\,,\,\alpha_2) - \alpha_3\, u_{3,\alpha_2}^i(\alpha_1\,,\,\alpha_2)\\
\bar{u}_3(\alpha_1\,,\,\alpha_2) &= u_3^i(\alpha_1\,,\,\alpha_2)
\end{aligned} \tag{35}$$

where u_1^i, u_2^i, and u_3^i represent the components of displacement over the thickness of the shell at the ith nodal position. Hence, the kinematic relations for stiffeners are obtained

$$\begin{aligned}
\varepsilon_1 &= \frac{\partial u_2^i}{\partial\alpha_2} + \frac{1}{2}\left(\frac{\partial u_3^i}{\partial\alpha_2}\right)^2 + \frac{u_3^i}{R} - \alpha_3\left(\frac{\partial^2 u_3^i}{\partial{\alpha_2}^2}\right)\\
\varepsilon_2 &= \frac{\partial u_1^i}{\partial\alpha_1} + \frac{1}{2}\left(\frac{\partial u_3^i}{\partial\alpha_1}\right)^2 - \alpha_3\left(\frac{\partial^2 u_3^i}{\partial{\alpha_1}^2}\right)
\end{aligned} \tag{36}$$

where ε_1 and ε_2 denote the axial and circumferential strains. Consequently, the strain energy for circumferential and axial stiffeners are

given by:

$$U_r = \frac{1}{2W_r}\int_0^L\int_0^{R\Phi}\left[\left(\frac{u_3^i}{R}+\frac{1}{2}\left(\frac{\partial u_3^i}{\partial\alpha_2}\right)^2 + E_rA_r\left(\frac{\partial u_2^i}{\partial\alpha_2}\right)+E_r\left(\frac{b_r{d_r}^3}{12}+\left(\frac{h+h_r}{2}\right)^2A_r\right)\left(\frac{\partial^2 u_3^i}{\partial{\alpha_2}^2}\right)^2\right)^2 - E_rA_r(h+h_r)\left(\frac{\partial^2{u_3}^i}{\partial{\alpha_2}^2}\right)\left(\frac{\partial{u_2}^i}{\partial\alpha_2}+\frac{1}{2}\left(\frac{\partial{u_3}^i}{\partial\alpha_2}\right)^2+\frac{{u_3}^i}{R}\right) + G_r\frac{h_r{d_r}^3}{3}\left(\frac{\partial^2{u_3}^i}{\partial\alpha_1\partial\alpha_2}\right)^2\Bigg]d\alpha_2 d\alpha_1 \tag{37}$$

$$U_s = \frac{1}{2W_s}\int_0^L\int_0^{R\Phi}\left[\left(E_sA_s\left(\frac{\partial u_1^i}{\partial\alpha_1}\right)+\frac{1}{2}\left(\frac{\partial u_3^i}{\partial\alpha_1}\right)^2 + E_s\left(\frac{b_s{d_s}^3}{12}+\left(\frac{h+h_s}{2}\right)^2A_s\right)\left(\frac{\partial^2 u_3^i}{\partial{\alpha_1}^2}\right)^2\right)^2 - E_sA_s(h+h_s)\left(\frac{\partial^2 u_3^i}{\partial{\alpha_1}^2}\right)\left(\frac{\partial u_1^i}{\partial\alpha_1}+\frac{1}{2}\left(\frac{\partial u_3^i}{\partial\alpha_1}\right)^2\right) + G_s\frac{h_s{d_s}^3}{3}\left(\frac{\partial^2 u_3^i}{\partial\alpha_1\partial\alpha_2}\right)^2\Bigg]d\alpha_2 d\alpha_1 \tag{38}$$

where W_r and W_s represent ring and stringer spacing, respectively, and Φ denotes shell angle. E is the effective Young's modulus, and the subscripts r and s stand for ring and stringer stiffeners, respectively. Based on the stationary potential energy criterion, the equilibrium equations of the shell under mechanical loadings can be derived. To this end, first, the expression for the overall potential energy of the shell, which is strengthened by ring and stringer stiffeners, is provided as follows

$$\Pi = \Omega + U_r + U_s + U_o \tag{39}$$

where Ω denotes the potential energy of the mechanical loads, which is defined as the negative value of the work performed by mechanical loading during the deformation of the shell. Considering axial compressive edge load $N_{0\alpha_1}$ and lateral pressure $N_{0\alpha_2}$, the potential energy of the loading is expressed by

$$\Omega = \frac{1}{2}\int_0^L\int_0^{R\Phi}\left(N_{0\alpha_1}+N_{0\alpha_2}\right)\left((w_{,\alpha_1})^2+(v_{,\alpha_1})^2\right)d\alpha_2 d\alpha_1 \tag{40}$$

It is worthwhile noting that the impact of quadratic terms in Eq. (40) on the buckling of short- or medium-length shells is trivial. In particular, the reduction in length resulting from circumferential displacement can be disregarded for stiffened shells having a length-to-radius ratio ranging from 0.7 to 3 [87]. Furthermore, U_o represents the total strain energy of the shell provided by

$$U_o = \int_0^L\int_0^{R\Phi}\int_{-h2}^{h2}(\sigma_{11}\varepsilon_{11}+\sigma_{22}\varepsilon_{22}+\tau_{12}\gamma_{12}+\tau_{13}\gamma_{13}+\tau_{23}\gamma_{23}) \times d\alpha_3\, d\alpha_2\, d\alpha_1 \tag{41}$$

The equilibrium equations of shell may be derived by employing the Euler equations. It can be stated that a loaded shell attains equilibrium when its total potential energy, denoted by Π, remains constant. This state of equilibrium is achieved when the integrand in the expression for Π follows the Euler equations of the calculus of variations. The equilibrium equations of the shell are given in Appendix A.

The equations governing the stability of shells are derived by applying the principle of minimum potential energy. The transition from stable to neutral equilibrium occurs when the total potential energy expression no longer represents a relative minimum. The criterion for stability loss is met when the integrand in the second variation expression of Π satisfies the Euler equations of calculus of variations. This procedure will be explained in detail in the following. Employing Taylor series, the expansion of Π about the equilibrium state is given by

$$\Delta\Pi = \delta\Pi + \frac{1}{2}\delta^2\Pi + \frac{1}{6}\delta^3\Pi + \cdots \tag{42}$$

The first variation $\delta\Pi$ is related to the equilibrium state. The stability condition of the original configuration of the shell in the neighbourhood of the equilibrium state may be obtained by the sign of second variation $\delta^2\Pi$. The condition $\delta^2\Pi = 0$ can be applied to determine the stability equations of the buckling problem. To obtain the corresponding expression for the second variation of the total potential energy, let

$$u_1 = {u_1}^0 + {u_1}^1, \qquad u_2 = {u_2}^0 + {u_2}^1, \qquad u_3 = {u_3}^0 + {u_3}^1,$$
$$\phi_1 = {\phi_1}^0 + {\phi_1}^1, \qquad \phi_2 = {\phi_2}^0 + {\phi_2}^1 \tag{43}$$

where ${u_1}^0$, ${u_2}^0$, ${u_3}^0$, ${\phi_1}^0$, and ${\phi_2}^0$ denote the displacement fields of the equilibrium state. ${u_1}^1$, ${u_2}^1$, ${u_3}^1$, ${\phi_1}^1$, and ${\phi_2}^1$ are a virtual increment in the displacement fields, i.e. at the neighbourhood of the stable equilibrium. The stress resultants are comprised of two components that express the stable equilibrium and the neighbouring condition. Additionally, the critical buckling is determined by mechanical loading applied to the original shell configuration, provided that the variation equation $\delta^2\Pi = 0$ is met. By calculating the second variation of the potential and utilizing the Euler equations, the stability equations can be derived, as presented in Appendix B.

3. Numerical solution

Since the stability equations of the shell, Eqs. (A.1)–(A.6), cannot be solved analytically, consequently, an efficient combined numerical technique is employed to determine the critical buckling load. To this end, first, the Levy method is employed to seek a solution that satisfies the simply supported boundary conditions, and thereby reduces the 2-D problem to a 1-D problem with respect to the coordinate α_1. Afterwards, the generalized differential quadrature (GDQ) technique is used to discretize the governing equations. It has been deemed that the forces $N^0_{\alpha_1\alpha_1}$ and $N^0_{\alpha_2\alpha_2}$ in α_1 and α_2 directions, respectively, may are given by

$$N^0_{\alpha_1\alpha_1} = -\frac{F_{\alpha_1}}{2\pi R}, \qquad N^0_{\alpha_2\alpha_2} = -F_{\alpha_2}R, \qquad \kappa = \frac{F_{\alpha_2}}{2\pi R^2 F_{\alpha_1}} \tag{44}$$

With consideration of the simply supported boundary conditions at the two edges of the shells as:

$$u_2^1 = u_3^1 = M^1_{\alpha_1\alpha_1} = N^1_{\alpha_1\alpha_1} = \phi_2^1 = 0 \qquad at \quad \alpha_1 = 0, L \tag{45}$$

In the Levy procedure, the following representation of the displacement are assumed

$$\begin{aligned}
\bar{u}_1 &= \sum_{n=1}^{\infty}\underline{u}_1(\alpha_1)\sin(\beta_m\alpha_2)\\
\bar{u}_2 &= \sum_{n=1}^{\infty}\underline{u}_2(\alpha_1)\cos(\beta_m\alpha_2)\\
\bar{u}_3 &= \sum_{n=1}^{\infty}\underline{u}_3(\alpha_1)\sin(\beta_m\alpha_2)\\
\bar{\phi}_1 &= \sum_{n=1}^{\infty}\underline{\phi}_1(\alpha_1)\sin(\beta_m\alpha_2)\\
\bar{\phi}_2 &= \sum_{n=1}^{\infty}\underline{\phi}_2(\alpha_1)\cos(\beta_m\alpha_2)
\end{aligned} \tag{46}$$

where $\beta_m = m\pi\Phi$, and m =1, 2, … denotes the number of half waves in α_2-direction. The partial differential equations (PDEs) obtained by

Table 1
Comparison of the critical buckling loads of thin unstiffened graded closed cylindrical shells with aligned and straight CNTs (T= 300 K, $\Phi = 2\pi$, h = 1mm, $R/h = 100$, $\overline{Z} = L^2/Rh$.

	$V_c^* = 0.12$		$V_c^* = 0.17$		$V_c^* = 0.28$	
	Uniform	Sandglass	Uniform	Sandglass	Uniform	Sandglass
$\overline{Z} = 100$						
Ref. [88]	18.75	21.81	30.43	35.53	37.77	47.18
Present work	19.82	22.93	31.572	36.45	39.01	48.80
$\overline{Z} = 300$						
Ref. [88]	19.35	22.06	31.11	37.06	39.60	46.52
Present work	20.00	23.33	32.09	38.13	40.55	48.87
$\overline{Z} = 500$						
Ref. [88]	18.72	21.37	30.57	35.14	37.31	45.99
Present work	19.91	22.14	32.11	36.46	38.29	46.80

substituting Eq. (46) into Eqs. (A.1)–(A.6) are discretized using the GDQ method. The comprehensive overview of the GDQ approach can be found in [75,89]. In compact vector notation, the discretized form of PDEs obtained together with related boundary conditions elaborated in Eq. (45) is expressed as

$$\begin{bmatrix} [K_{bb}] & [K_{bd}] \\ [K_{db}] & [K_{dd}] \end{bmatrix} \begin{Bmatrix} \delta_b \\ \delta_d \end{Bmatrix} + F \begin{bmatrix} 0 & 0 \\ [K_{g1}] & [K_{g2}] \end{bmatrix} \begin{Bmatrix} \delta_b \\ \delta_d \end{Bmatrix} = 0 \tag{47}$$

where the subscripts d and b represent domain and boundary, respectively. Indeed, the sub-matrices $[K_{bb}]$, $[K_{bd}]$, $[K_{db}]$, and $[K_{dd}]$ are components of the stiffness matrix that pertain to boundary and domain conditions. Furthermore, $[K_{g_1}]$ and $[K_{g_2}]$ are considered as sub-matrices when taking into account the influence of external force and the imposed conditions on the boundaries and domain. It should be noted that δ_b and δ_d represent the degrees of freedom associated with the boundary and domain, respectively. These degrees of freedom are defined as follows

$$\{\delta_d\} = \left\{ \underline{u}_{1i} \quad \underline{u}_{2i} \quad \underline{u}_{3i} \quad \underline{\phi}_{1i} \quad \underline{\phi}_{2i} \right\}^T \qquad i = 2, \ldots, N-1 \tag{48}$$

and

$$\{\delta_b\} = \left\{ \{\Gamma_1\} \quad \{\Gamma_N\} \right\}^T \tag{49}$$

where

$$\{\Gamma_i\} = \left\{ \underline{u}_{1i} \quad \underline{u}_{2i} \quad \underline{u}_{3i} \quad \underline{\phi}_{1i} \quad \underline{\phi}_{2i} \right\}^T \qquad i = 1, N \tag{50}$$

In order to convert Eq. (47) into the standard eigenvalue equation, it is necessary to eliminate the vector $\{\delta_b\}$. The vector $\{\delta_b\}$ can be obtained from Eq. (47) using the following expression

$$\{\delta_b\} = [K_{bb}]^{-1}[K_{bd}]\{\delta_d\} \tag{51}$$

By back-substituting Eq. (51) into Eq. (47), the following expression is derived

$$\begin{aligned} &[K_{dd}]\{\delta_d\} - [K_{db}][K_{bb}]^{-1}[K_{bd}]\{\delta_d\} \\ &\quad + F\left(-[K_{g1}][K_{db}][K_{bb}]^{-1}[K_{bd}]\{\delta_d\} + [K_{g2}]\{\delta_d\}\right) = 0 \end{aligned} \tag{52}$$

Eq. (52) can be transformed into an eigenvalue problem in the following manner

$$\begin{aligned} &\left(-[K_{g1}][K_{db}][K_{bb}]^{-1}[K_{bd}] + [K_{g2}]\right)^{-1} \left(-[K_{db}][K_{bb}]^{-1}[K_{bd}]\right. \\ &\quad \left. + [K_{dd}]\right)\{\delta_d\} + F\{\delta_d\} = 0 \end{aligned} \tag{53}$$

Eventually, the critical buckling load, denoted as F, is determined by solving Eq. (53).

4. Numerical results and discussion

4.1. Validation

Due to lack of appropriate results for mechanical buckling of the shell for direct comparison, validation of the present methodology is carried out in two ways. Initially, in the context of continuously graded closed cylindrical shells, the precision of the current numerical work utilizing two-parameter EMT is evaluated against that presented in Ref. [88] which employed an extended rule of mixture and graded aligned, straight CNTs. In Table 1, Poly (methyl methacrylate), named as PMMA, has been selected for the matrix phase while the (10, 10) SWCNTs have been considered as reinforcements. Moreover, at a proposed temperature of T = 300 K, which is equivalent to room temperature, there are no thermal strains. As can be seen in this table, there is an excellent agreement between the results verifying the accuracy of the present numerical work. It is interesting to note that for two types of CNTs profiles, the critical mechanical buckling load determined using the EMT is higher than that determined using the extended rule of mixture for various CNTs volume fractions.

Table 2
Comparison of the critical buckling loads of unstiffened and stiffened isotropic closed cylindrical shell ($L = R = 0.3$).

R/h	Unstiffened		Stiffened	
	Present work	Ref. [90]	Present work	Ref. [90]
30	26.4529	26.2390	26.5272	26.3023
100	2.3891	2.3615	2.4076	2.3659
200	0.5981	0.5904	0.6086	0.5988
300	0.2663	0.2623	0.2730	0.2672

Secondly, the results are contrasted with those obtained from isotropic closed cylindrical shells. This study centres on the critical buckling load of closed cylindrical shells made of alumina-based isotropic material, both stiffened and unstiffened, as discussed in Ref. [90]. As shown in Table 2, the results presented in this comparison for different values of mid-radius to thickness are in good agreement.

4.2. Mechanical buckling analysis of porous nanocomposite shells

Having assessed the validity of the current methodology, a number of test cases including different class of structures, ranging from closed to open CGP shells, with or without exterior and interior stiffening elements, different geometrical parameters, and various types of material profiles, are presented. The investigated shell experiences a concurrent application of lateral pressure and axial compressive load. The methodology developed here, indeed, has a broad variety of applications and may be effectively used to do exploratory research on many sorts of design. Aside from showcasing the potential application to a range of design possibilities, this section intends to presenting the high efficiency and fast rate of convergence of the method by presenting the results to establish its very high accuracy and versatility.

For all findings discussed in this section, the buckling load intensity factor (BLIF) is represented by

$$\text{BLIF} = F_{cr} L^2 D \pi^2 \tag{54}$$

where $D = E_m h^3/12\left(1-\upsilon_m{}^2\right)$ denotes the rigidity modulus of the shell. The (10,10) SWCNTs as the reinforcement phase and copper as the metal matrix [91,92] are selected. The material properties of metal matrix (copper) are E_m = 130 GPa and υ_m = 0.34. According

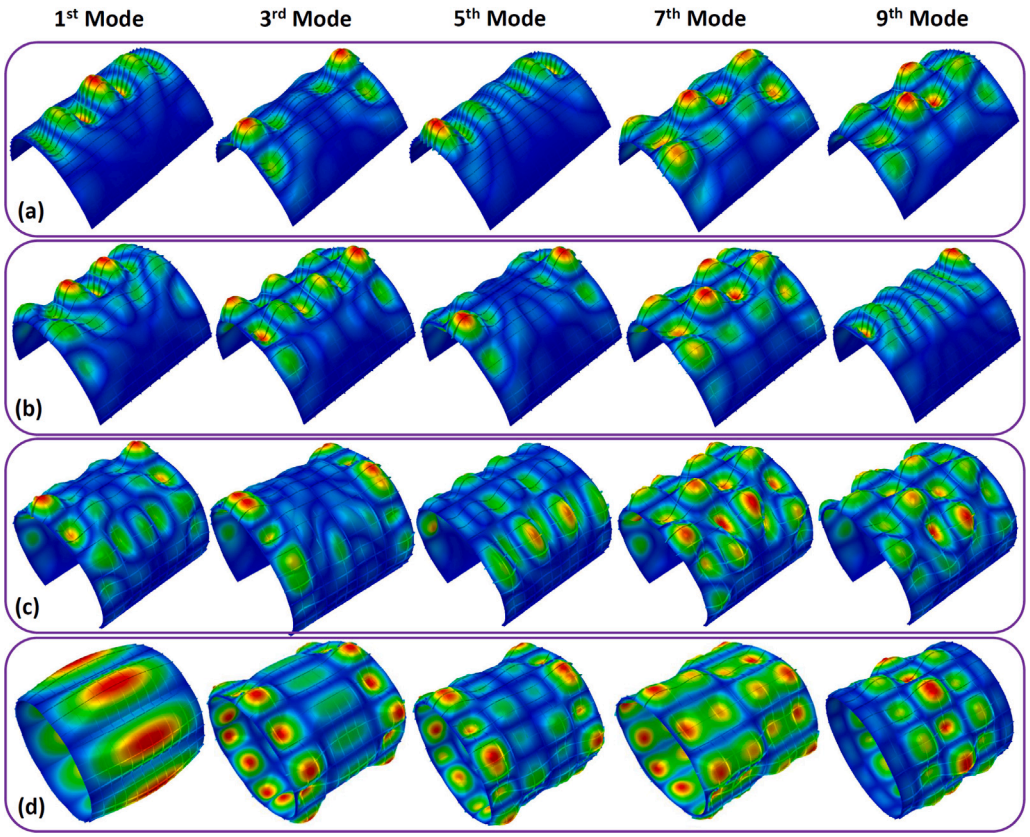

Fig. 5. Buckling mode shapes of CGP shells with different shell angle for Classic porosity distribution and Sandglass CNTs profile ($L/R = 1$, $R/h = 50$, $N_r = 11$, $N_s = 23$). In this example, the ABAQUS FE models use the first-order shell element S4R as a general-purpose shell element with six degrees of freedom per node. **(a)** $\Phi = 3\pi/4$. **(b)** $\Phi = \pi$. **(c)** $\Phi = 3\pi/R = 2$. **(d)** $\Phi = 2\pi$.

to the molecular dynamics simulation results predicted by Shen and Zhang [93], the material properties of the (10,10) SWCNTs are $E_c^{11} = 5.6466$ TPa, $E_c^{22} = 7.06$ TPa, $G_c^{12} = 1.9445$ TPa, and $\upsilon_c^{22} = 0.175$ at room temperature (300 K) and the effective wall thickness is 0.067 nm satisfying the Vodenitcharova–Zhang criterion [94]. All the computations reported in this section are carried out by considering $V_c^* = 0.28$ unless the otherwise mentioned.

The purpose of this part is to demonstrate the precision of the approach via comparison with both benchmark data and FEM computations. In this work, ABAQUS FE code version 6.17 [95] is used. The FE models use the first-order shell element S4R as a general-purpose shell element with six degrees of freedom per node (three displacements and three rotations). The mesh density is determined through a preliminary convergence analysis, with an average component size of 5 mm. It is of significance to mention that FE analyses have been conducted employing both the shell element S4R and the solid continuum element C3D8R. However, for the purpose of conciseness, the outcomes of the continuum element have not been included in this work. It is crucial to highlight that upon comparing the results of both element types, the S4R element exhibits superior computational efficiency, but the differences in outcomes are minimal. This determination is underpinned by the understanding that using solid continuum elements becomes progressively uneconomical when the R/h ratio surpasses 25 [96,97]. Table 3 presents a summary of the results obtained for the CGP shells using the methodology proposed in this study and FEM. In contrast to FEM, the discrepancies observed in the comparison remain negligible, with a maximum deviation of approximately 1%. Figs. 5 and 6 show different buckling mode shapes of the CGP shells with different number of shell angle and stiffeners, respectively.

To attain an accurate BLIF of the CGP, a series of calculations are conducted to ascertain the necessary quantity of grid points along the longitudinal axis of the shell. A convergence study of the numerical results for CGP shells with Sandglass CNTs profile is shown in Figs. 7 and 8 for different values of the mid-radius to thickness ratio, R/h, and the aggregation parameter, γ, respectively. The results are obtained by setting $a = 1$, $b = 1$, $\zeta = 2$, and $\xi_p = 1$. As observed in these figures, not only the numerical method converges very fast as the number of grid points in the longitudinal direction rises, but it also shows that using only 9 number of grid points one can gain accurate BLIF for the shell. It is worthwhile noting that with the escalation of the aggregation parameter, γ, resulting in a reduction of the CNTs agglomeration within the metal matrix, there is an observable enhancement in the convergence behaviour.

Figs. 9a and 9b show the variation of the BLIF of the CGP shell with the length-to-mean radius ratio, L/R, different types of CNTs distribution profiles, and porosity dispersion. It can be observed from these figures that, on the one hand, the BLIF is significantly influenced in that the BLIF increases steadily as L/R ratio becomes larger, manifesting that a longer shell possesses a higher critical buckling load. On the other hand, it is interesting to note that the through-thickness variation of CNTs distribution according to the Sandglass type leads to a higher BLIF among other CNTs dispersion types. Comparing Symmetric and Asymmetric porosity distribution in Figs. 9a and 9b, respectively, shows that the discrepancy between the Uniform and Pyramid types of CNTs dispersion becomes more tangible for lower values of the L/R ratio. Moreover, the type of CNTs distribution within the matrix through the thickness of the shell has a noticeable impact of the BLIF in higher values of the L/R ratio, irrespective of how the porosity is distributed through the shell's radial direction.

The effect of the parameter ξ_p on the buckling behaviour of the CGP stiffened shell is compared in Figs. 10a and 10b for different porosity distribution profiles. The porosity distribution governed by

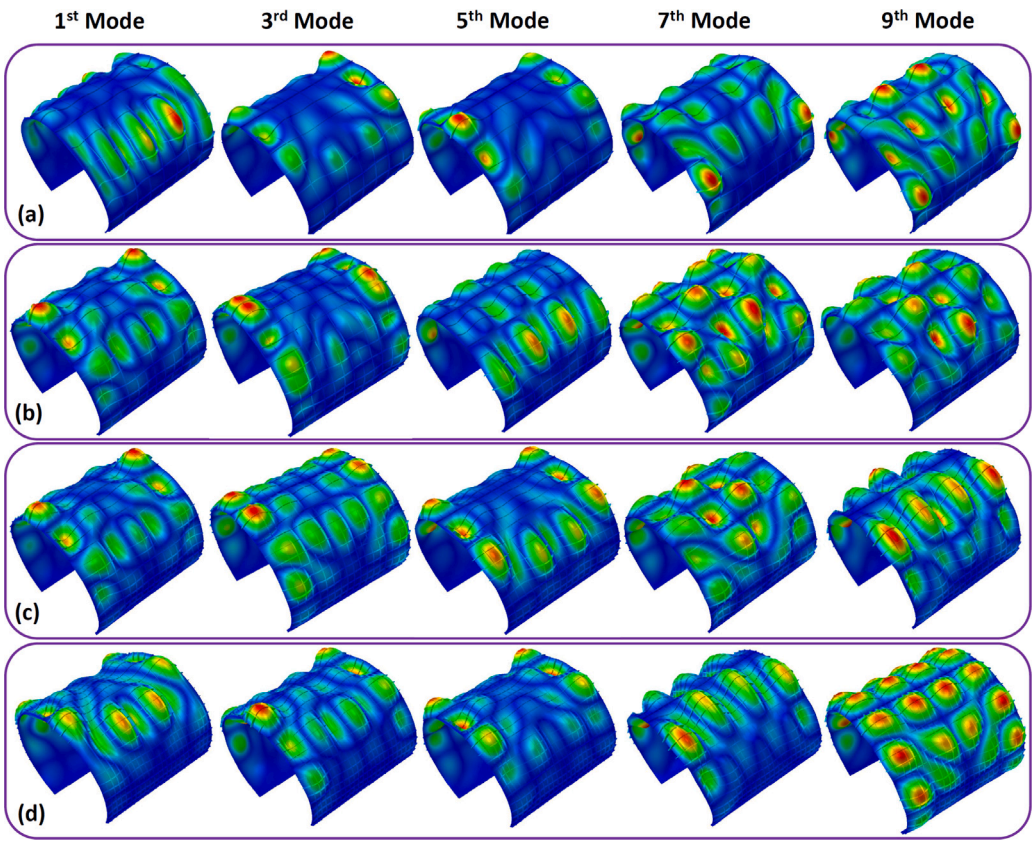

Fig. 6. Buckling mode shapes of CGP shells with different number of stiffeners for Classic porosity distribution and Sandglass CNTs profile. ($L/R = 1$, $R/h = 50$, $\Phi = 3\pi/2$). **(a)** $N_r = 7$, $N_s = 15$. **(b)** $N_r = 11$, $N_s = 23$. **(c)** $N_r = 17$, $N_s = 31$. **(d)** $N_r = 23$, $N_s = 35$.

Table 3
Comparison of the critical buckling loads of stiffened CGP shells with different shell angle and mode shapes for Classic porosity distribution and Sandglass profile ($R/h = 50$, $L/R = 1$, $N_r = N_s = 25$).

Angle		1st	3rd	5th	7th	9th
$3\pi/4$	Present work	190.4228	213.7297	248.0652	459.5321	464.4831
	FEM	191.5183	215.0001	249.2951	460.4457	465.9151
π	Present work	145.3471	162.1929	189.0039	357.8868	364.0761
	FEM	146.8507	163.0004	189.9992	359.0158	365.5249
$3\pi/2$	Present work	97.9643	109.0456	128.7471	244.3276	250.7626
	FEM	99.0002	110.2924	130.0025	245.3459	251.4428
2π	Present work	73.7549	82.0260	97.2818	184.9379	189.4963
	FEM	74.4490	83.0004	98.0249	185.7751	190.3751

Eq. (23) can be influenced through the appropriate choice of the parameter ξ_p. It has been explained in Ref. [74] that the tendency of CNTs to aggregate more in the inclusions has a detrimental impact on the mechanical buckling behaviour of cylindrical shells. This trend has been also observed in this figure. Comparing Figs. 10a and 10b reveals that for different agglomeration degrees of CNTs within the metal matrix, the porosity distributions symmetrically with respect to the mid-surface of the shell has a remarkable impact on the buckling behaviour of the CGP shell. However, when it comes to Classic porosity distribution, the parameter ξ_p has a negligible effect on the BLIF of the CGP shell. Another point that can stand out from Fig. 10b is that the change in the parameter ξ_p and, as a result, the symmetric distribution of the porosity is much more appreciable on the buckling behaviour of the CGP shell when the agglomeration degree of the CNTs is more sever. This will be more investigated in the next tables.

Effect of number of ring and stringer stiffeners on the buckling load intensity factor of CGP shells with varying the parameter ξ_p and the length-to-mean radius ratio for Classic and Symmetric porosity Profiles is investigated in Tables 4 and 5. Certain significant findings evident from these tables are as follows: (*i*) For various types of porosity distribution profiles, the buckling load intensity factor rises with the number of stiffeners. (*ii*) By increasing the parameter ξ_p for Classic porosity profile, the BLIF slightly drops, whilst for Symmetric porosity profile it is the other way round. This is attributed to different distributions of porosities and, as a result, the Young's modulus of the shell in relation to the mid-surface in Classic and Symmetric Profiles. (*iii*) In comparison to shells stiffened by interior stiffeners, those stiffened by exterior stiffeners have greater critical buckling loads.

Fig. 11 represents the comparison of the buckling behaviour of continuously graded Symmetric, Asymmetric, and Classic porous shells with three different CNTs distributions. It can be inferred from this figure that the impact of different CNTs distribution profiles on the BILF of the stiffened shell is noticeably higher than those of various porosity dispersion profiles. This highlights the proper selection of the grade CNTs distributions through the shell's thickness. Furthermore, as can be seen from this figure, symmetrical distribution of porosities leads to an improvement in the buckling behaviour of the shell, followed by the Asymmetric profile. In other words, porosities distributed close to the mid-surface are more effective in increasing the stiffness of the structure than other non-uniform porosities distributions, Classic or Asymmetric profiles. Therefore, designers can obtain desired stiffness

Table 4
Effect of number of ring and stringer stiffeners on the buckling load intensity factor of CGP shells with varying the parameter ξ_p and the length-to-mean radius ratio for Classic porosity Profile. ($R/L = 2, \Phi = 2\pi/3, \gamma = \delta = 0.5, a = 1, b = 0$).

R/h		N_i[a] = 6		$N_i = 15$		$N_i = 24$	
		10	100	10	100	10	100
Interior stiffeners							
$\xi_p =$	0	166.9023	514.5110	166.9055	514.8749	166.9087	515.2385
	0.5	166.8990	514.5012	166.9023	514.8651	166.9055	515.2282
	1	166.8958	514.4914	166.8991	514.8552	166.9023	515.2184
	3	166.8939	514.4855	166.8971	514.8493	166.9004	515.2125
	5	166.8914	514.4776	166.8946	514.8415	166.8978	515.2047
Exterior stiffeners							
$\xi_p =$	0	166.9672	517.8356	167.0677	523.1757	167.1683	528.5023
	0.5	166.9640	517.8258	167.0645	523.1660	167.1651	528.4926
	1	166.9608	517.8160	167.0613	523.1562	167.1619	528.4829
	3	166.9588	517.8102	167.0594	523.1504	167.1600	689.1948
	5	166.9563	517.8024	167.0569	523.1426	167.1574	528.4771

[a] $i = r$ or s .

Table 5
The buckling load intensity factor of CGP shells with varying number of ring and stringer stiffeners, the parameter ξ_p, and the length-to-mean radius ratio for Symmetric porosity Profile. ($R/L = 2$, $\Phi = 2\pi/3$, $\gamma = \delta = 0.5$, $a = 1$, $b = 1$, $\zeta = 2$).

R/h		N_i[a] = 6		$N_i = 15$		$N_i = 24$	
		10	100	10	100	10	100
Interior stiffeners							
$\xi_p =$	0	166.9023	514.5110	166.9055	514.8749	166.9087	515.2381
	0.5	193.8203	597.4526	193.8240	597.9074	193.8277	598.3614
	1	222.7263	683.9032	222.7308	684.4574	222.7354	685.0106
	3	237.2923	713.8565	233.1400	714.4445	233.1449	715.0314
	5	237.2923	725.2776	237.2974	725.8776	237.3025	726.4765
Exterior stiffeners							
$\xi_p =$	0	166.9672	517.8356	167.0677	523.1757	167.1683	528.5023
	0.5	193.8793	193.8793	193.9714	605.3693	194.0635	610.2871
	1	222.7795	686.5788	222.8640	691.1400	222.9484	695.6923
	3	233.1864	716.4345	233.2684	720.8834	233.3504	725.3241
	5	237.3430	727.8214	237.4240	732.2311	237.5051	736.6327

[a] $i = r$ or s .

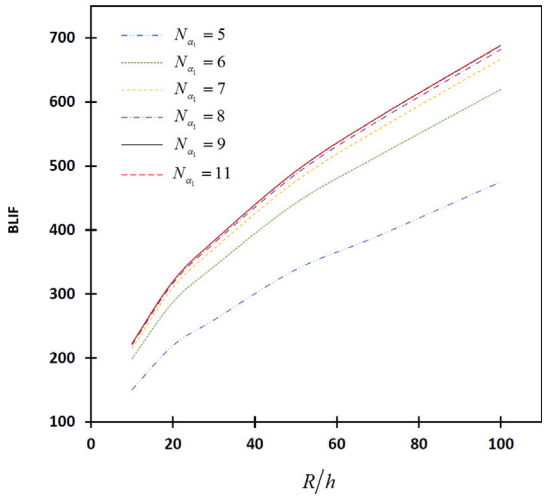

Fig. 7. Convergence of the buckling load intensity factor versus the mid-radius to thickness ratio, R/h, of CGP shells with Sandglass CNTs profile. As evident from these figures, the numerical approach not only exhibits rapid convergence as the longitudinal grid points increase in number but also underscores the possibility of achieving accurate BLIF for the shell using a minimal count of 9 grid points. ($L/R = 2$, $\Phi = 2\pi/R = 2$, $N_r = N_s = 10$, $a = 1$, $b = 1$, $\zeta = 2$, $\xi_p = 1$).

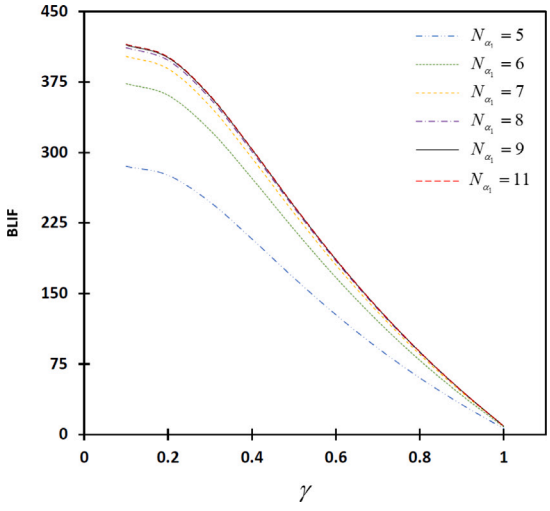

Fig. 8. Convergence of the buckling load intensity factor versus the aggregation parameter, γ, of CGP shells with Sandglass CNTs profile. As depicted in this figure, with the increase of the aggregation parameter denoted as γ, leading to a reduction in the agglomeration of CNTs within the metal matrix, there is an observable improvement in the convergence behaviour. ($L/R = 2$, $R/h = 20$, $\Phi = \pi/2$, $N_r = N_s = 15$, $a = 1$, $b = 1$, $\zeta = 2$, $\xi_p = 1$).

and buckling behaviour of CGP shells by regulating distributions of CNTs as well as porosities through the thickness of structure.

In order to scrutinize the impact of the agglomeration parameter δ used in the EMT approach on the buckling behaviour of CGP stiffened shells, variation of the BLIF with the parameter δ for different porosities and CNTs distribution profiles is shown in Fig. 12. As explained in Eq. (2), by increasing the parameter δ the agglomeration degree of CNTs within the metal matrix drops and, as a result, the BLIF of the shell gradually grows, followed by higher growth rate for greater values of the parameter δ. It is interesting to note that the appropriate choice

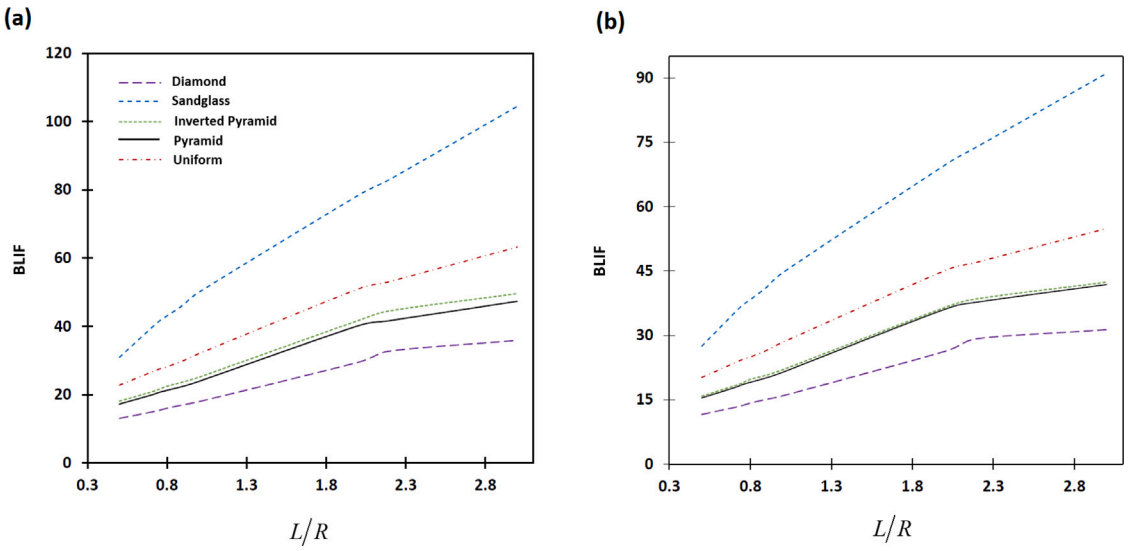

Fig. 9. Variation of the buckling load intensity factor of CGP shells with the length-to-mean radius ratio, L/R, for different types of CNTs distribution profiles. As discerned from the figure, the manner in which CNTs are distributed within the matrix across the shell's thickness exerts a notable influence on the BLIF for elevated values of the L/R ratio, independent of the mode of porosity distribution along the radial direction of the shell. ($R/h = 10$, $\Phi = 2\pi$, $N_r = N_s = 20$, $\delta = \gamma = 0.5$, $\zeta = 2$, $\xi_p = 1$). **(a)** Symmetric profile ($a = 1$, $b = 1$). **(b)** Asymmetric profile ($a = 1$, $b = 0.5$).

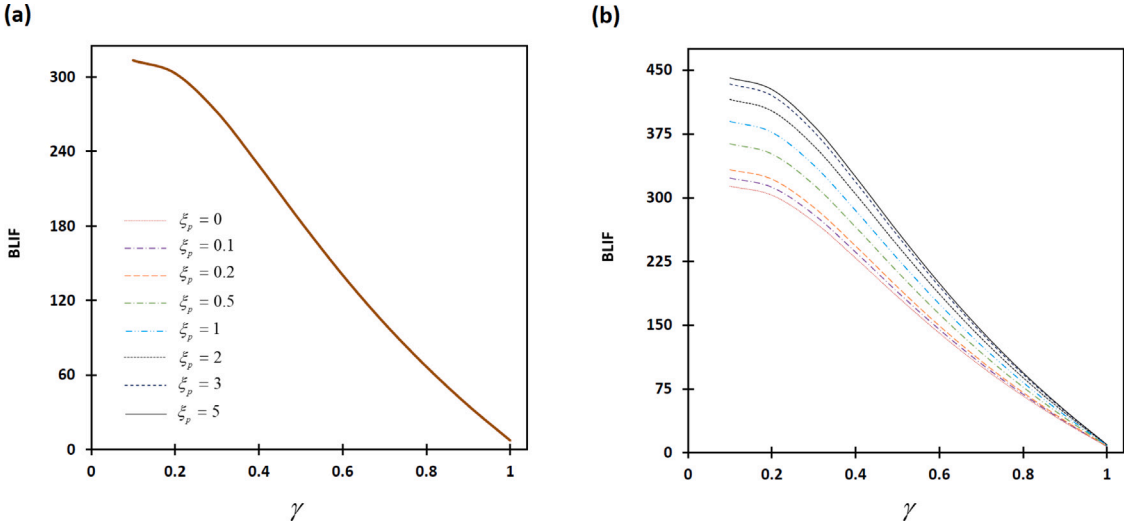

Fig. 10. Effect of the parameter ξ_p on the buckling behaviour of the CGP stiffened shell for different agglomeration degrees of CNTs. As evident, for varying degrees of CNT agglomeration within the metal matrix, the porosity distributions that exhibit symmetry relative to the mid-surface of the shell profoundly influence the buckling behaviour of the CGP shell. ($R/h = 20$, $L/R = 2$, $\Phi = \pi/2$, $N_r = N_s = 15$, $\delta = 0.1$, $\zeta = 2$). **(a)** Classic profile ($a = 1$, $b = 0$). **(b)** Symmetric profile ($a = 1$, $b = 1$).

of CNTs and porosities distribution profiles through the thickness plays a crucial role in the buckling behaviour of the shell with the lower degree of CNTs agglomeration. The BLIF of the CGP shell with Symmetric and Asymmetric porosity profiles increases by 32% and 18%, respectively, than that of Classic profile.

Fig. 13 shows the variation of the BLIF with the shell angle for two values of the mid-radius to thickness ratio, $R/h = 10$ and $R/h = 50$ and different porosities distribution profiles. As can be seen in this figure, overall, the BLIF of both R/h ratios declines by increasing the shell angle irrespective of the type of porosity profile. However, the BLIF of shells with lower values of the R/h ratio slumps as $\Phi < 100$, whilst the downturn for thicker shells follows a mild trend and then remains almost unaltered for closed shells. The impacts of the agglomeration parameter γ and CNTs profiles on the variation of the BLIF with the shell angle are studied in Fig. 14. It is found that the discrepancy in the buckling behaviour of CGP shells with different CNTs profiles substantially increases by reducing the agglomeration degree of CNTs dispersed within the metal matrix phase. This trend is more appreciable in smaller values of the shell angle.

5. Conclusion

This study has introduced a numerical model to investigate the buckling behaviour of bio-inspired CGP nanocomposite cylindrical shells. These shells were constructed using metal foams with closed-cell structures characterized by power-law distributed porosity profiles. By incorporating an elastic isotropic metal matrix containing dispersed elastic CNTs, the study considered the impact of CNTs agglomeration using the EMT approach to derive the effective constitutive law. The focus was on understanding the effects of geometrical parameters, porosity variability, and CNTs distribution on the buckling performance of CGP shells, thereby offering insights for designing enhanced stability in closed-cell cellular stiffened shells. Through the application of the adjacent equilibrium criterion, the stability equations were solved

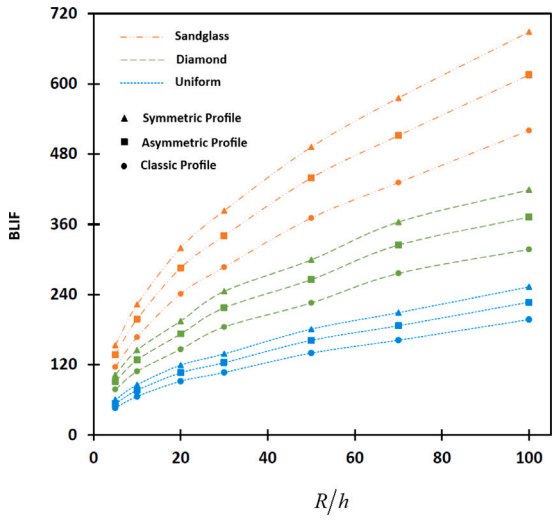

Fig. 11. Comparison of the buckling behaviour of continuously graded Symmetric, Asymmetric, and Classic porous shells with three different CNTs distributions. It can be discerned from this figure that the influence of distinct CNTs distribution profiles on the BLIF of the stiffened shell is markedly more pronounced compared to the effects stemming from diverse porosity dispersion profiles. ($L/R = 2$, $\Phi = 2\pi/3$, $N_r = N_s = 10$, $\xi_p = 1$, $\delta = \gamma = 0.5$).

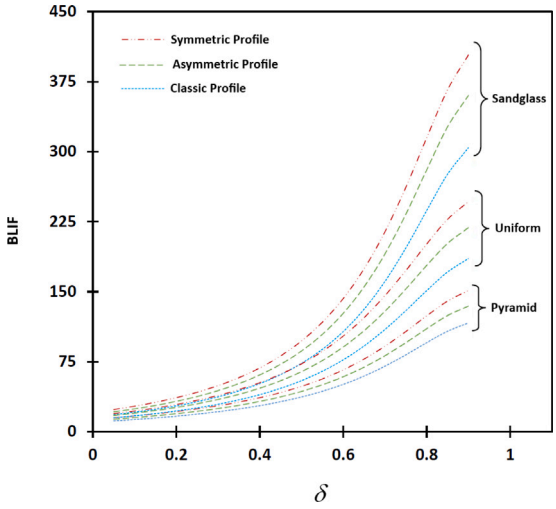

Fig. 12. Variation of BLIF with agglomeration parameter δ for different porosities and CNTs distribution profiles. The appropriate selection of distribution profiles for CNTs and porosities throughout the thickness assumes a pivotal role in influencing the buckling behaviour of the shell, particularly when dealing with a lower degree of CNTs agglomeration. In comparison to the Classic profile, the BLIF of the CGP shell experiences a notable increase of 32% with the adoption of the Symmetric porosity profile and an 18% increase with the utilization of the Asymmetric porosity profile. ($R/h = 20$, $L/R = 2$, $\Phi = \pi/2$, $N_r = N_s = 15$, $\xi_p = 1$, $\gamma = 0.95$).

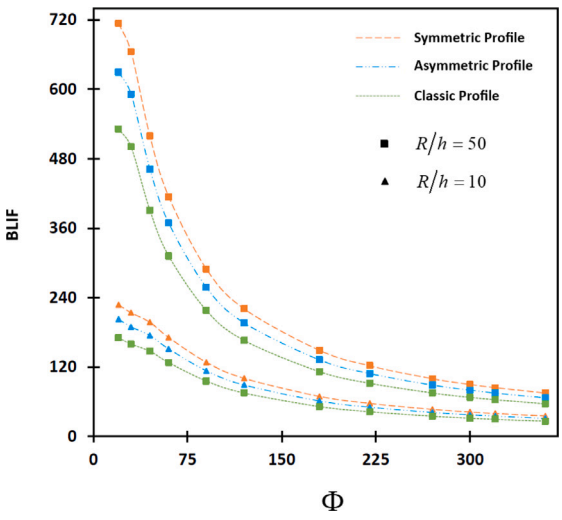

Fig. 13. BLIF versus shell angle for different values of mid-radius to thickness ratio and porosities distribution profiles. As evident from the this figure, the BLIF for both R/h ratios decreases with an increasing shell angle, regardless of the porosity profile. However, for shells with lower R/h ratios and $\Phi < 100$, the BLIF experiences a significant decline. In contrast, the BLIF for thicker shells exhibits a gradual decline, stabilizing for closed shells. ($L/R = 2$, $\delta = 0.2$, $\gamma = 0.7$, $N_r = N_s = 10$).

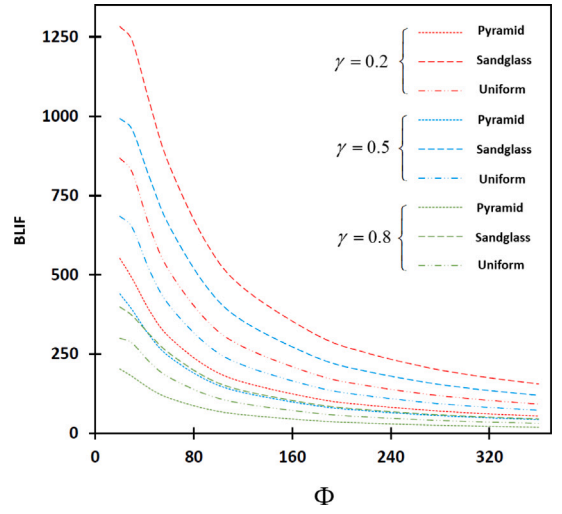

Fig. 14. Variation of BLIF with shell angle for different values of agglomeration parameter γ and CNTs profiles. It can be observed from this figure that the disparity in the buckling behaviour of CGP shells with varying CNTs profiles is notably amplified by diminishing the degree of CNTs agglomeration dispersed within the metal matrix phase. ($R/h = 40$, $L/R = 2$, $\delta = 0.2$, $N_r = N_s = 20$, $a = 1$, $b = 1$, $\zeta = 2$).

employing the GDQ and Levy techniques. The results have contributed substantially to the field by providing fundamental knowledge that serves as a basis for developing cellular stiffened shells exhibiting optimal porosity and CNTs distributions, consequently leading to improved stability.

The primary findings underscored the pivotal role of CNTs distribution within the matrix on the enhancement of the BLIF for higher L/R ratios. Furthermore, the symmetric distribution of porosity around the mid-surface significantly influenced the buckling behaviour, particularly when dealing with varying degrees of CNTs agglomeration. Notably, the controlling porosity parameter (ξ_p) displayed minimal impact on buckling behaviour when employing a Classic porosity distribution. In addition, the strategic allocation of porosities closer to the mid-surface, in contrast to alternative non-uniform distributions, effectively heightened the stiffness of the structure. The study further disclosed that the deviation in buckling characteristics became more pronounced as the degree of CNTs agglomeration decreased within the metallic matrix phase, a trend more noticeable for lower shell angles.

This work has contributed valuable insights towards the design of CGP shells with amplified stability and structural resilience. The findings laid out in this study set the stage for future endeavours in optimizing lightweight and robust composite structures that harness the synergistic potential of both CNTs and porosity distributions.

CRediT authorship contribution statement

B. Sobhani Aragh: Writing – original draft, Software, Methodology, Investigation, Conceptualization, Formal analysis, Software, Validation, Visualization, Supervision, Writing – review & editing. **W. Tan:** Writing – review & editing, Writing – original draft, Methodology, Investigation, Conceptualization, Visualization. **E. Borzabadi Farahani:** Writing – review & editing, Software, Formal analysis, Validation, Writing – original draft. **M. Al-Greer:** Writing – review & editing, Supervision, Resources, Writing – original draft. **D. Hughes:** Writing – review & editing, Supervision, Investigation, Resources, Writing – original draft.

Declaration of competing interest

The authors declare that they have no known competing financial interests or personal relationships that could have appeared to influence the work reported in this paper.

Data availability

No data was used for the research described in the article

Acknowledgments

W. Tan acknowledges the financial support from the EPSRC (grant No. EP/V049259/1).

Appendix A

The equilibrium equations of the CGP shell can be obtained as follow

$$\frac{\partial N_{\alpha_1\alpha_1}}{\partial\alpha_1}+\frac{\partial N_{\alpha_1\alpha_2}}{\partial\alpha_2}+\frac{\partial}{\partial\alpha_1}\left[\frac{1}{W_s}\left(E_sA_s\left(\frac{\partial u_1^i}{\partial\alpha_1}+\frac{1}{2}\left(\frac{\partial u_1^i}{\partial\alpha_1}\right)^2\right)-A_sE_sH_s\left(\frac{\partial u_3^i}{\partial\alpha_1}\right)^2\right)\right]=0 \tag{A.1}$$

$$\frac{\partial N_{\alpha_1\alpha_2}}{\partial\alpha_1}+\frac{\partial N_{\alpha_2\alpha_2}}{\partial\alpha_2}+\frac{\partial}{\partial\alpha_2}\left[\frac{1}{W_r}\left(E_rA_r\left(\frac{\partial u_2^i}{\partial\alpha_2}+\frac{u_3^i}{R}+\frac{1}{2}\left(\frac{\partial u_3^i}{\partial\alpha_2}\right)^2\right)-A_rE_rH_r\left(\frac{\partial^2u_3^i}{\partial{\alpha_2}^2}\right)\right)\right]=0 \tag{A.2}$$

$$\begin{aligned}
&-\frac{1}{R}N_{\alpha_2\alpha_2}-\frac{1}{RW_r}\left(E_rA_r\left(\frac{\partial u_2^i}{\partial\alpha_2}+\frac{u_3^i}{R}+\frac{1}{2}\left(\frac{\partial u_3^i}{\partial\alpha_2}\right)^2\right)-A_rE_rH_r\left(\frac{\partial^2u_3^i}{\partial{\alpha_2}^2}\right)\right)\\
&+N_{\alpha_1\alpha_1}\left(\frac{\partial^2u_3}{\partial{\alpha_1}^2}\right)\\
&+N_{\alpha_2\alpha_2}\frac{\partial^2u_3}{\partial{\alpha_2}^2}+2N_{\alpha_1\alpha_2}\frac{\partial^2u_3}{\partial\alpha_1\partial\alpha_2}+N_{0\alpha_2}\frac{\partial^2u_3}{\partial{\alpha_2}^2}+\frac{1}{W_s}\bar{N}_{\alpha_1\alpha_1}\frac{\partial^2u_3^i}{\partial{\alpha_1}^2}-\\
&+N_{0\alpha_1}\frac{\partial^2u_3}{\partial{\alpha_1}^2}+\frac{1}{W_r}\bar{N}_{\alpha_2\alpha_2}\frac{\partial^2u_3}{\partial{\alpha_2}^2}+\frac{\partial Q_{\alpha_1\alpha_3}}{\partial\alpha_1}+\frac{\partial Q_{\alpha_2\alpha_3}}{\partial\alpha_2}\\
&+4h^2\left(\frac{\partial R_{\alpha_1\alpha_3}}{\partial\alpha_1}+\frac{\partial R_{\alpha_2\alpha_3}}{\partial\alpha_2}\right)\\
&-\frac{4h^2}{3}\left(\frac{\partial^2P_{\alpha_1\alpha_1}}{\partial{\alpha_1}^2}+2\frac{\partial^2P_{\alpha_1\alpha_2}}{\partial\alpha_1\alpha_2}+\frac{\partial^2P_{\alpha_2\alpha_2}}{\partial{\alpha_2}^2}\right)\\
&-\frac{\partial^2}{\partial{\alpha_1}^2}\left[\frac{1}{W_s}\left(\left(\left(E_sI_s-4E_sA_sH_s\frac{h^2}{3}\left(\frac{h}{2}\right)^4\right)\left(\frac{\partial^2u_3^i}{\partial{\alpha_1}^2}\right)\right)\right.\right.\\
&\left.\left.-\left(A_sE_sH_s+E_sA_s\frac{4h^2}{3}\left(\frac{h}{2}\right)^3\right)\left(\frac{\partial u_1^i}{\partial\alpha_1}+\frac{1}{2}\left(\frac{\partial u_3^i}{\partial\alpha_1}\right)^2\right)\right)\right]\\
&-\frac{\partial^2}{\partial{\alpha_2}^2}\left[\frac{1}{W_r}\left(\left(E_rI_r-E_rA_rH_r\frac{4h^2}{3}\left(\frac{h}{2}\right)^3\right)\right.\right.\\
&\left.\left.\left(\frac{\partial^2u_3^i}{\partial{\alpha_2}^2}\right)-\left(A_rE_rH_r-E_rA_r\frac{4h^2}{3}\left(\frac{h}{2}\right)^3\right)\left(\frac{\partial u_2^i}{\partial\alpha_2}+\frac{1}{2}\left(\frac{\partial u_3^i}{\partial\alpha_2}\right)^2+\frac{u_3^i}{R}\right)\right)\right]\\
&-\frac{\partial^2}{\partial\alpha_1\partial\alpha_2}\left[\frac{1}{W_s}\left(G_sJ_s\frac{\partial^2u_3^i}{\partial\alpha_1\partial\alpha_2}\right)\right.\\
&\left.+\frac{1}{W_r}\left(G_rJ_r\frac{\partial^2u_3^i}{\partial\alpha_1\partial\alpha_2}\right)\right]=0
\end{aligned} \tag{A.3}$$

$$\begin{aligned}
&-Q_{\alpha_1\alpha_3}-4h^2R_{\alpha_1\alpha_3}+\frac{\partial M_{\alpha_1\alpha_1}}{\partial{\alpha_1}^2}+\frac{\partial M_{\alpha_1\alpha_2}}{\partial{\alpha_2}^2}-\frac{4h^2}{3}\left(\frac{\partial P_{\alpha_1\alpha_1}}{\partial{\alpha_1}^2}+\frac{\partial P_{\alpha_1\alpha_2}}{\partial{\alpha_2}^2}\right)\\
&+\frac{\partial}{\partial\alpha_1}\left[\frac{1}{W_s}\left(E_sA_s\left(\frac{h}{2}+\right.\right.\right.\\
&\left.\left.\left.+\frac{4h^2}{3}\left(\frac{h}{2}\right)^2\right)+\left(\frac{\partial u_1^i}{\partial\alpha_1}+\frac{1}{2}\left(\frac{\partial u_3^i}{\partial\alpha_1}\right)^2\right)\right.\right.\\
&\left.\left.-A_sE_sH_s\left(\frac{h}{2}+\frac{4h^2}{3}\left(\frac{h}{2}\right)^3\right)\left(\frac{\partial^2u_3^i}{\partial{\alpha_1}^2}\right)\right)\right]=0
\end{aligned} \tag{A.4}$$

$$\begin{aligned}
&-Q_{\alpha_2\alpha_3}-4h^2R_{\alpha_2\alpha_3}+M_{\alpha_1\alpha_2,\alpha_1}+\frac{\partial M_{\alpha_2\alpha_2}}{\partial\alpha_2}+\frac{4h^2}{3}\left(\frac{\partial P_{\alpha_1\alpha_2}}{\partial\alpha_2}+\frac{\partial P_{\alpha_2\alpha_2}}{\partial\alpha_2}\right)\\
&+\frac{\partial}{\partial\alpha_2}\left[\frac{1}{W_r}\left(E_rA_r\left(\frac{h}{2}+\right.\right.\right.\\
&\left.\left.\left.+\frac{4h^2}{3}\left(\frac{h}{2}\right)^3\right)+\left(\frac{\partial u_2^i}{\partial\alpha_2}+\frac{u_3^i}{R}+\frac{1}{2}\left(\frac{\partial u_3^i}{\partial\alpha_2}\right)^2\right)\right.\right.\\
&\left.\left.-A_rE_rH_r\left(\frac{h}{2}+\frac{4h^2}{3}\left(\frac{h}{2}\right)^3\right)\left(\frac{\partial^2u_3^i}{\partial{\alpha_2}^2}\right)\right)\right]=0
\end{aligned} \tag{A.5}$$

where $\bar{N}_{\alpha_1\alpha_1}$ and $\bar{N}_{\alpha_2\alpha_2}$ are the mechanical forces applied to the ring and stringer stiffeners expressed by:

$$\begin{aligned}
\bar{N}_{\alpha_1\alpha_1}&=E_sA_s\left(\frac{\partial u_1^i}{\partial\alpha_1}+\frac{1}{2}\left(\frac{\partial u_3^i}{\partial\alpha_1}\right)^2\right)-A_sE_sH_s\left(\frac{\partial^2u_3^i}{\partial{\alpha_1}^2}\right)\\
\bar{N}_{\alpha_2\alpha_2}&=E_rA_r\left(\frac{\partial u_2^i}{\partial\alpha_2}+\frac{1}{2}\left(\frac{\partial u_3^i}{\partial\alpha_2}\right)^2+\frac{u_3^i}{R}\right)-A_rE_rH_r\left(\frac{\partial^2u_3^i}{\partial{\alpha_2}^2}\right)
\end{aligned} \tag{A.6}$$

Appendix B

The stability equations can be further explained in the following manner

$$\frac{\partial N^1_{\alpha_1\alpha_1}}{\partial\alpha_1}+\frac{\partial N^1_{\alpha_1\alpha_2}}{\partial\alpha_2}+\frac{\partial}{\partial\alpha_1}\left[\frac{1}{W_s}\left(E_sA_s\frac{\partial {u_1^i}^1}{\partial\alpha_1}-A_sE_sH_s\frac{\partial^2{u_3^i}^1}{\partial{\alpha_1}^2}\right)\right]=0 \tag{B.1}$$

$$\frac{\partial N^1_{\alpha_1\alpha_2}}{\partial\alpha_1}+\frac{\partial N^1_{\alpha_2\alpha_2}}{\partial\alpha_2}+\frac{\partial}{\partial\alpha_2}\left[\frac{1}{W_r}\left(E_rA_r(\frac{\partial {u_2^i}^1}{\partial\alpha_2}+\frac{{u_3^i}^1}{R})-A_rE_rH_r(\frac{\partial^2{u_3^i}^1}{\partial{\alpha_2}^2})\right)\right]=0 \tag{B.2}$$

$$\begin{aligned}
&\frac{1}{R}N^1_{\alpha_2\alpha_2}-\frac{1}{RW_r}\left(E_rA_r(\frac{\partial {u_2^i}^1}{\partial\alpha_2}+\frac{{u_3^i}^1}{R})-E_rA_rH_r(\frac{\partial^2{u_3^i}^1}{\partial{\alpha_2}^2})\right)+\\
&N^{\frac{\partial^2{u_1}^1}{\partial{\alpha_1}^2}}_{\alpha_1\alpha_1}+2N^0_{\alpha_1\alpha_2}\frac{\partial^2u_3{}^1}{\partial\alpha_1\partial\alpha_2}+\frac{1}{W_s}\bar{N}^0_{\alpha_1\alpha_1}\frac{\partial^2{u_3^i}^1}{\partial{\alpha_1}^2}+\frac{1}{W_r}\bar{N}^0_{\alpha_2\alpha_2}\frac{\partial^2{u_3^i}^1}{\partial{\alpha_2}^2}+
\end{aligned}$$

$$N_{\alpha_2\alpha_2}^{\frac{\partial^2 u_3^1}{\partial \alpha_2^2}} + Q_{\alpha_1\alpha_3}^1 + Q_{\alpha_2\alpha_3}^1 + 4h^2\left(\frac{\partial R_{\alpha_1\alpha_3}^1}{\partial \alpha_1} + R_{\alpha_2\alpha_3}^1\right) - \frac{4h^2}{3}\left(\frac{\partial^2 P_{\alpha_1\alpha_1}^1}{\partial {\alpha_1}^2} + 2\frac{\partial^2 P_{\alpha_1\alpha_2}^1}{\partial \alpha_1 \partial \alpha_2} + \frac{\partial^2 P_{\alpha_2\alpha_2}^1}{\partial {\alpha_2}^2}\right) - \frac{\partial^2}{\partial {\alpha_1}^2}\left[\frac{1}{W_s}\left(\frac{\partial^2 {u_3^i}^1}{\partial {\alpha_1}^2}\left(E_s I_s - E_s A_s H_s \frac{4h^2}{3}\left(\frac{h}{2}\right)^3\right) - \frac{\partial {u_1^i}^1}{\partial \alpha_1}\left(E_s A_s H_s - E_s A_s \frac{4h^2}{3}\left(\frac{h}{2}\right)^3\right)\right)\right] - \frac{\partial^2}{\partial {\alpha_2}^2}\left[\frac{1}{W_r}\left(\frac{\partial^2 {u_3^i}^1}{\partial {\alpha_2}^2}\left(E_r I_r - E_r A_r H_r \frac{4h^2}{3}\left(\frac{h}{2}\right)^3\right) - \left(\frac{\partial {u_2^i}^1}{\partial \alpha_2} + \frac{{u_3^i}^1}{R}\right)\left(E_r A_r H_r - E_r A_r H_r \frac{4h^2}{3}\left(\frac{h}{2}\right)^3\right)\right)\right]$$

$$\frac{\partial^2}{\partial \alpha_1 \partial \alpha_2}\left[\frac{1}{W_s} G_s J_s \frac{\partial^2 {u_3^i}^1}{\partial \alpha_1 \partial \alpha_2} + \frac{1}{W_r} G_r J_r \frac{\partial^2 {u_3^i}^1}{\partial \alpha_1 \partial \alpha_2}\right] = 0 \tag{B.3}$$

$$-Q_{\alpha_1\alpha_3}^1 - 4h^2 R_{\alpha_1\alpha_3}^1 + \frac{\partial M_{\alpha_1\alpha_1}^1}{\partial \alpha_1} + \frac{\partial M_{\alpha_1\alpha_2}^1}{\partial \alpha_2} + \frac{4h^2}{3}\left(\frac{\partial P_{\alpha_1\alpha_1}^1}{\partial \alpha_1} + \frac{\partial P_{\alpha_1\alpha_2}^1}{\partial \alpha_2}\right) + \frac{\partial}{\partial \alpha_1}\left[\frac{1}{W_s}\left(E_s A_s \frac{\partial {u_3^i}^1}{\partial \alpha_1}\left(\frac{h}{2} + \frac{4h^2}{3}\left(\frac{h}{2}\right)^3\right) - A_s E_s H_s \frac{\partial {u_3^i}^1}{\partial \alpha_1}\left(\frac{h}{2} + \frac{4h^2}{3}\left(\frac{h}{2}\right)^3\right)\right)\right] = 0 \tag{B.4}$$

$$-Q_{\alpha_2\alpha_3}^1 + 4h^2 R_{\alpha_2\alpha_3}^1 + \frac{\partial M_{\alpha_1\alpha_2}^1}{\partial \alpha_1} + \frac{\partial M_{\alpha_2\alpha_2}^1}{\partial \alpha_2} - \frac{4h^2}{3}\left(\frac{\partial P_{\alpha_1\alpha_2}^1}{\partial \alpha_2} + \frac{\partial P_{\alpha_2\alpha_2}^1}{\partial \alpha_2}\right) + \frac{\partial}{\partial \alpha_2}\left[\frac{1}{W_r}\left(E_r A_r\left(\frac{\partial {u_2^i}^1}{\partial \alpha_2} + \frac{{u_3^i}^1}{R}\right)\left(\frac{h}{2} + \frac{4h^2}{3}\left(\frac{h}{2}\right)^3\right) + E_r A_r H_r \frac{\partial^2 {u_3^i}^1}{\partial {\alpha_2}^2}\left(\frac{h}{2} + \frac{4h^2}{3}\left(\frac{h}{2}\right)^3\right)\right)\right] = 0 \tag{B.5}$$

In the context of force resultants, the stability state is denoted by a superscript 1 and the equilibrium state is denoted by a superscript 0. The prebuckling force resultants $N_{\alpha_1\alpha_1}^0$ and $N_{\alpha_2\alpha_2}^0$ are obtained from Eqs. (A.1)–(A.6).

References

[1] Cao S, Ma N, Zhang Y, Bo R, Lu Y. Fabrication, mechanical properties, and multifunctionalities of particle reinforced foams: A review. Thin-Walled Struct 2023;186:110678.

[2] Choi Y, Ahn T-Y, Ha S-H, Lee J-I, Cho J-H. Electrochemical properties of a lithium-impregnated metal foam anode (LIMFA FeCrAl) for molten salt thermal batteries. Sci Rep 2022;12(1):4474.

[3] Zhang Z, Chen Y, Sun S, Sun K, Sun H, Li H, et al. Recent progress on three-dimensional nanoarchitecture anode materials for lithium/sodium storage. J Mater Sci Technol 2022.

[4] Ma X, Jing Z, Feng C, Qiao M, Xu D. Research and development progress of porous foam-based electrodes in advanced electrochemical energy storage devices: A critical review. Renew Sustain Energy Rev 2023;173:113111.

[5] Wan T, Liu Y, Zhou C, Chen X, Li Y. Fabrication, properties, and applications of open-cell aluminum foams: A review. J Mater Sci Technol 2021;62:11–24.

[6] Du Plessis A, Razavi SMJ, Benedetti M, Murchio S, Leary M, Watson M, et al. Properties and applications of additively manufactured metallic cellular materials: A review. Prog Mater Sci 2022;125:100918.

[7] Banhart J. Manufacture, characterisation and application of cellular metals and metal foams. Prog Mater Sci 2001;46(6):559–632.

[8] Ahankari SS, Kar KK. Functionally graded composites: Processing and applications. Compos Mater: Process Appl Charact 2017;119–68.

[9] Kokkinis D, Bouville F, Studart AR. 3D printing of materials with tunable failure via bioinspired mechanical gradients. Adv Mater 2018;30(19):1705808.

[10] Naebe M, Shirvanimoghaddam K. Functionally graded materials: A review of fabrication and properties. Appl Mater Today 2016;5:223–45.

[11] Mirzaali M, De La Nava AH, Gunashekar D, Nouri-Goushki M, Veeger R, Grossman Q, et al. Mechanics of bioinspired functionally graded soft-hard composites made by multi-material 3D printing. Compos Struct 2020;237:111867.

[12] Miserez A, Schneberk T, Sun C, Zok FW, Waite JH. The transition from stiff to compliant materials in squid beaks. Science 2008;319(5871):1816–9.

[13] Martin RB. Porosity and specific surface of bone. Crit Rev Biomed Eng 1984;10(3):179–222.

[14] Chen D, Yang J, Schneider J, Kitipornchai S, Zhang L. Impact response of inclined self-weighted functionally graded porous beams reinforced by graphene platelets. Thin-Walled Struct 2022;179:109501.

[15] Dong Y, Li Y, Chen D, Yang J. Vibration characteristics of functionally graded graphene reinforced porous nanocomposite cylindrical shells with spinning motion. Composites B 2018;145:1–13.

[16] Zghal S, Dammak F. Vibration characteristics of plates and shells with functionally graded pores imperfections using an enhanced finite shell element. Comput Math Appl 2021;99:52–72.

[17] Zghal S, Ataoui D, Dammak F. Static bending analysis of beams made of functionally graded porous materials. Mech Based Des Struct Mach 2022;50(3):1012–29.

[18] Zghal S, Trabelsi S, Dammak F. Transient response of functionally graded porous plate. In: Advances in materials, mechanics and manufacturing II: proceedings of the third international conference on advanced materials, mechanics and manufacturing. Springer; 2022, p. 150–5.

[19] Zghal S, Ataoui D, Dammak F. Free vibration analysis of porous beams with gradually varying mechanical properties. Proc Inst Mech Eng Part M: J Eng Mar Environ 2022;236(3):800–12.

[20] Zghal S, Joueid N, Tornabene F, Dimitri R, Chrigui M, Dammak F. Time-dependent deflection responses of FG porous structures subjected to different external pulse loads. J Vib Eng Technol 2023;1–20.

[21] Banhart J, García-Moreno F, Heim K, Seeliger H-W. Light-weighting in transportation and defence using aluminium foam sandwich structures. Light Weight Defense Aerospace Transp 2019;61–72.

[22] García-Moreno F. Commercial applications of metal foams: Their properties and production. Materials 2016;9(2):85.

[23] Avey M, Fantuzzi N, Sofiyev A. On the solution of thermal buckling problem of moderately thick laminated conical shells containing carbon nanotube originating layers. Materials 2022;15(21):7427.

[24] Sofiyev A. Review of research on the vibration and buckling of the FGM conical shells. Compos Struct 2019;211:301–17.

[25] Sofiyev A, Schnack E. The stability of functionally graded cylindrical shells under linearly increasing dynamic torsional loading. Eng Struct 2004;26(10):1321–31.

[26] Avey M, Fantuzzi N, Sofiyev A. Mathematical modeling and analytical solution of thermoelastic stability problem of functionally graded nanocomposite cylinders within different theories. Mathematics 2022;10(7):1081.

[27] Sofiyev AH, Fantuzzi N. Stability analysis of shear deformable inhomogeneous nanocomposite cylindrical shells under hydrostatic pressure in thermal environment. Materials 2023;16(13):4887.

[28] Ipek C, Sofiyev A, Fantuzzi N, Efendiyeva SP, et al. Buckling behavior of nanocomposite plates with functionally graded properties under compressive loads in elastic and thermal environments. J Appl Comput Mech 2023.

[29] Duc ND, Seung-Eock K, Khoa ND, Chan DQ. Nonlinear buckling and post-buckling analysis of shear deformable stiffened truncated conical sandwich shells with functionally graded face sheets and a functionally graded porous core. J Sandwich Struct Mater 2021;23(7):2700–35.

[30] Zhou Z, Ni Y, Tong Z, Zhu S, Sun J, Xu X. Accurate nonlinear buckling analysis of functionally graded porous graphene platelet reinforced composite cylindrical shells. Int J Mech Sci 2019;151:537–50.

[31] Nam VH, Trung N-T, et al. Buckling and postbuckling of porous cylindrical shells with functionally graded composite coating under torsion in thermal environment. Thin-Walled Struct 2019;144:106253.

[32] Allahkarami F, Saryazdi MG, Tohidi H. Dynamic buckling analysis of bi-directional functionally graded porous truncated conical shell with different boundary conditions. Compos Struct 2020;252:112680.

[33] Twinkle C, Pitchaimani J. Free vibration and stability of graphene platelet reinforced porous nano-composite cylindrical panel: Influence of grading, porosity and non-uniform edge loads. Eng Struct 2021;230:111670.

[34] Zghal S, Dammak F. Buckling responses of porous structural components with gradient power-based and sigmoid material variations under different types of compression loads. Compos Struct 2021;273:114313.

[35] Thai D-K, Tu TM, Hoa LK, Hung DX, Linh NN, et al. Nonlinear stability analysis of eccentrically stiffened functionally graded truncated conical sandwich shells with porosity. Materials 2018;11(11):2200.

[36] Shahgholian D, Safarpour M, Rahimi A, Alibeigloo A. Buckling analyses of functionally graded graphene-reinforced porous cylindrical shell using the Rayleigh–Ritz method. Acta Mech 2020;231(5):1887–902.

[37] Tao C, Dai T. Isogeometric analysis for postbuckling of sandwich cylindrical shell panels with graphene platelet reinforced functionally graded porous core. Compos Struct 2021;260:113258.
[38] Novozhilov VV. Foundations of the nonlinear theory of elasticity. London: Constable and Company; 1999.
[39] Mindlin RD. Influence of Rotatory Inertia and Shear on Flexural Motions of Isotropic, Elastic Plates. J Appl Mech 2021;18(1):31–8.
[40] Reissner E. The effect of transverse shear deformation on the bending of elastic plates. J Appl Mech USA 1945;A69–77.
[41] Hencky H. Über die Berücksichtigung der Schubverzerrung in ebenen Platten. Ingenieur-Arch 1947;16(1):72–6.
[42] Whitney J, Sun C. A higher order theory for extensional motion of laminated composites. J Sound Vib 1973;30(1):85–97.
[43] Hanna N, Leissa A. A higher order shear deformation theory for the vibration of thick plates. J Sound Vib 1994;170(4):545–55.
[44] Lo K, Christensen R, Wu E. A high-order theory of plate deformation—Part 1: Homogeneous plates. 1977.
[45] Reddy J. A refined nonlinear theory of plates with transverse shear deformation. Int J Solids Struct 1984;20(9–10):881–96.
[46] Reddy JN. Mechanics of laminated composite plates and shells: theory and analysis. CRC Press; 2003.
[47] Sobhani Aragh B, Borzabadi Farahani E, Xu B, Ghasemnejad H, Mansur W. Manufacturable insight into modelling and design considerations in fibre-steered composite laminates: State of the art and perspective. Comput Methods Appl Mech Engrg 2021;379:113752.
[48] Vescovini R, Fantuzzi N. Free vibrations of conical shells via Ritz method. Int J Mech Sci 2023;241:107925.
[49] Cha SI, Kim KT, Arshad SN, Mo CB, Hong SH. Extraordinary strengthening effect of carbon nanotubes in metal-matrix nanocomposites processed by molecular-level mixing. Adv Mater 2005;17(11):1377–81.
[50] Al-Aqeeli N. Processing of CNTs reinforced Al-based nanocomposites using different consolidation techniques. J Nanomater 2013;2013.
[51] Bradbury CR, Gomon J-K, Kollo L, Kwon H, Leparoux M. Hardness of multi wall carbon nanotubes reinforced aluminium matrix composites. J Alloys Compd 2014;585:362–7.
[52] Sun Y, Sun J, Liu M, Chen Q. Mechanical strength of carbon nanotube–nickel nanocomposites. Nanotechnology 2007;18(50):505704.
[53] Kang N, Coddet P, Liu Q, Liao H, Coddet C. In-situ TiB/near α Ti matrix composites manufactured by selective laser melting. Addit Manuf 2016;11:1–6.
[54] Zhou W, Sun X, Kikuchi K, Nomura N, Yoshimi K, Kawasaki A. Carbon nanotubes as a unique agent to fabricate nanoceramic/metal composite powders for additive manufacturing. Mater Des 2018;137:276–85.
[55] Gu DD, Meiners W, Wissenbach K, Poprawe R. Laser additive manufacturing of metallic components: Materials, processes and mechanisms. Int Mater Rev 2012;57(3):133–64.
[56] Qiu C, Kindi MA, Aladawi AS, Hatmi IA. A comprehensive study on microstructure and tensile behaviour of a selectively laser melted stainless steel. Sci Rep 2018;8(1):1–16.
[57] Gu D, Rao X, Dai D, Ma C, Xi L, Lin K. Laser additive manufacturing of carbon nanotubes (CNTs) reinforced aluminum matrix nanocomposites: Processing optimization, microstructure evolution and mechanical properties. Addit Manuf 2019;29:100801.
[58] Yu T, Liu J, He Y, Tian J, Chen M, Wang Y. Microstructure and wear characterization of carbon nanotubes (CNTs) reinforced aluminum matrix nanocomposites manufactured using selective laser melting. Wear 2021;476:203581.
[59] Yin H, Yang J, Zhang Y, Crilly L, Jackson RL, Lou X. Carbon nanotube (CNT) reinforced 316L stainless steel composites made by laser powder bed fusion: Microstructure and wear response. Wear 2022;496:204281.
[60] Gkikas G, Barkoula N-M, Paipetis A. Effect of dispersion conditions on the thermo-mechanical and toughness properties of multi walled carbon nanotubes-reinforced epoxy. Composites B 2012;43(6):2697–705.
[61] Talò M, Krause B, Pionteck J, Lanzara G, Lacarbonara W. An updated micromechanical model based on morphological characterization of carbon nanotube nanocomposites. Composites B 2017;115:70–8.
[62] Sofiyev A, Kuruoglu N. Buckling analysis of shear deformable composite conical shells reinforced by CNTs subjected to combined loading on the two-parameter elastic foundation. Def Technol 2022;18(2):205–18.
[63] Alizada A, Sofiyev A. Modified Young's moduli of nano-materials taking into account the scale effects and vacancies. Meccanica 2011;46:915–20.
[64] Alizada A, Sofiyev A, Kuruoglu N. Stress analysis of a substrate coated by nanomaterials with vacancies subjected to uniform extension load. Acta Mech 2012;223(7):1371–83.
[65] Zghal S, Frikha A, Dammak F. Mechanical buckling analysis of functionally graded power-based and carbon nanotubes-reinforced composite plates and curved panels. Composites B 2018;150:165–83.
[66] Zghal S, Frikha A, Dammak F. Static analysis of functionally graded carbon nanotube-reinforced plate and shell structures. Compos Struct 2017;176:1107–23.
[67] Zghal S, Frikha A, Dammak F. Free vibration analysis of carbon nanotube-reinforced functionally graded composite shell structures. Appl Math Model 2018;53:132–55.
[68] Frikha A, Zghal S, Dammak F. Finite rotation three and four nodes shell elements for functionally graded carbon nanotubes-reinforced thin composite shells analysis. Comput Methods Appl Mech Engrg 2018;329:289–311.
[69] Zghal S, Frikha A, Dammak F. Non-linear bending analysis of nanocomposites reinforced by graphene-nanotubes with finite shell element and membrane enhancement. Eng Struct 2018;158:95–109.
[70] Zghal S, Frikha A, Dammak F. Large deflection response-based geometrical nonlinearity of nanocomposite structures reinforced with carbon nanotubes. Appl Math Mech 2020;41:1227–50.
[71] Zghal S, Trabelsi S, Dammak F. Post-buckling behavior of functionally graded and carbon-nanotubes based structures with different mechanical loadings. Mech Based Des Struct Mach 2022;50(9):2997–3039.
[72] Sobhani Aragh B, Barati AN, Hedayati H. Eshelby–Mori–Tanaka approach for vibrational behavior of continuously graded carbon nanotube-reinforced cylindrical panels. Composites B 2012;43(4):1943–54.
[73] Mehrabadi SJ, Sobhani Aragh B. Stress analysis of functionally graded open cylindrical shell reinforced by agglomerated carbon nanotubes. Thin-Walled Struct 2014;80:130–41.
[74] Sobhaniaragh B, Nejati M, Mansur W. Buckling modelling of ring and stringer stiffened cylindrical shells aggregated by graded CNTs. Composites B 2017;124:120–33.
[75] Sobhani Aragh B. Vibration and thermal stress analyses of functionally graded materials [Ph.D. thesis], Ghent University; 2014.
[76] He S-y, Lv Y-n, Chen S-t, Dai G, Liu J-g, Huo M-k. Gradient regulation and compressive properties of density-graded aluminum foam. Mater Sci Eng A 2020;772:138658.
[77] Gross D, Seelig T. Fracture mechanics: with an introduction to micromechanics. Springer; 2017.
[78] Eshelby JD. The determination of the elastic field of an ellipsoidal inclusion, and related problems. Proc R Soc Lond Ser A. Math Phys Sci 1957;241(1226):376–96.
[79] Mori T, Tanaka K. Average stress in matrix and average elastic energy of materials with misfitting inclusions. Acta Metall 1973;21(5):571–4.
[80] Benveniste Y. A new approach to the application of Mori-Tanaka's theory in composite materials. Mech Mater 1987;6(2):147–57.
[81] Gross D, Seelig T. Micromechanics and homogenization. In: Fracture mechanics. Springer; 2018, p. 243–319.
[82] Jalali S, Beigrezaee M, Pugno NM. Reporting a misunderstanding in relating the Young's modulus to functionally graded porosity. Compos Struct 2022;281:115007.
[83] Moradi-Dastjerdi R, Behdinan K. Free vibration response of smart sandwich plates with porous CNT-reinforced and piezoelectric layers. Appl Math Model 2021;96:66–79.
[84] Moradi-Dastjerdi R, Behdinan K. Dynamic performance of piezoelectric energy harvesters with a multifunctional nanocomposite substrate. Appl Energy 2021;293:116947.
[85] Moradi-Dastjerdi R, Behdinan K, Safaei B, Qin Z. Static performance of agglomerated CNT-reinforced porous plates bonded with piezoceramic faces. Int J Mech Sci 2020;188:105966.
[86] Roberts AP, Garboczi EJ. Computation of the linear elastic properties of random porous materials with a wide variety of microstructure. Proc R Soc Lond Ser A Math Phys Eng Sci 2002;458(2021):1033–54.
[87] Lim C, Ma Y, Kitipornchai S, Wang C, Yuen R. Buckling of vertical cylindrical shells under combined end pressure and body force. J Eng Mech 2003;129(8):876–84.
[88] Shen H-S. Postbuckling of nanotube-reinforced composite cylindrical shells in thermal environments, part I: Axially-loaded shells. Compos Struct 2011;93(8):2096–108.
[89] Groh R, Weaver PM, White S, Raju G, Wu Z. A 2D equivalent single-layer formulation for the effect of transverse shear on laminated plates with curvilinear fibres. Compos Struct 2013;100:464–78.
[90] Brush DO, Almroth BO, Hutchinson J. Buckling of bars, plates, and shells. 1975.
[91] Dong Y, He L, Wang L, Li Y, Yang J. Buckling of spinning functionally graded graphene reinforced porous nanocomposite cylindrical shells: An analytical study. Aerosp Sci Technol 2018;82:466–78.
[92] Kim KT, Cha SI, Hong SH, Hong SH. Microstructures and tensile behavior of carbon nanotube reinforced Cu matrix nanocomposites. Mater Sci Eng A 2006;430(1–2):27–33.
[93] Shen H-S, Zhang C-L. Thermal buckling and postbuckling behavior of functionally graded carbon nanotube-reinforced composite plates. Mater Des 2010;31(7):3403–11.
[94] Wang C, Zhang L. A critical assessment of the elastic properties and effective wall thickness of single-walled carbon nanotubes. Nanotechnology 2008;19(7):075705.
[95] Systèmes D. Abaqus analysis user's guide. In: Version 6.17, 2017. 2017.
[96] Sadowski AJ, Rotter JM. Solid or shell finite elements to model thick cylindrical tubes and shells under global bending. Int J Mech Sci 2013;74:143–53.
[97] Gantes CJ, Koulatsou KG, Chondrogiannis K-A. Alternative ring flange models for buckling verification of tubular steel wind turbine towers via advanced numerical analyses and comparison to code provisions. Structures 2023;47:1366–82.